Basin Modeling in the SF Bay Area – Final Project Report

U.S.G.S Award Number 04HQGR0062
Douglas S. Dreger
University of California, Berkeley, California, 94720
Ph. (510)643-1719; Fax (510)643-5811; dreger@seismo.berkeley.edu

Introduction

The development of 3D seismic velocity models is necessary for the simulation of strong ground motion for scenario earthquakes on the major faults of the San Francisco Bay Area. As 3D models are developed they need to be tested, validated and if necessary calibrated.

In this study we investigated the influence of sedimentary basin structure on the propagation of seismic waves in the Santa Clara Valley. We made use of teleseismic waveform data and spectral observations of micro-seismic noise recorded by the Santa Clara Valley Seismic Experiment (SCVSE, Lindh et al. 1999) to characterize the basin structure. The SCVSE was deployed for a 6-month period in 1998 during which time several small local earthquakes and numerous teleseisms were recorded. Additionally, this continuous recording network also recorded ambient noise, which can be used to characterize the seismic response of sedimentary basins. This work has resulted in two peer-reviewed publications (Dolenc et al., 2005; Dolenc and Dreger, 2005).

Additionally, we are developing a waveform inversion method to use these data to invert for updates to the 3D velocity model. The initial results of this effort were reported at the 2007 Seismological Society of America (SSA) meeting (Dolenc et al., 2007).

Approach

In order to find metrics with which to evaluate the 3D velocity structure we measured teleseismic P-wave arrival delays across the SCVSE as well as the relative amplitude, and wave energy. The various measures were related to values obtained for a site located outside the Santa Clara Valley and therefore the relative differences in times and amplitudes represents the effect of the basin structure. We then compared this parametric data to the basin depth of the UCB 3D model for the region (Stidham et al., 1999) and a preliminary USGS 3D model (Dolenc et al., 2005).

For the ambient noise observations we determined the maximum microseism spectral peak in the 0.1 to 1 Hz passband of the horizontal to vertical (H/V) spectral ratio, and correlated this dominant period with the reported basin depth and also the teleseismic measures described above.

We used a 3D elastic finite-difference method to simulate teleseismic and microseismic wavefields to model the observed behavior.

The details of these analyses are reported in Dolenc et al., (2005), and Dolenc and Dreger (2005), which are included in the appendix to this report.

We are in the process of developing a 3D waveform inversion method utilizing these data to update the velocity structure in the Santa Clara Valley. The preliminary results of this effort were reported at the 2007 SSA meeting (Dolenc et al., 2007), and are described in the results section of this report.

Results

Our analysis of teleseismic arrival time delays and relative amplification measured from sites of the SCVSE situated above the deep sedimentary basins of the Santa Clara Valley show that these measures are sensitive to the basin structure. We find that the teleseismic delay time observations are linearly correlated with the dominant period of the microseismic noise (Figure 1). This shows that the two data sets are sensitive to the same structure, and that they may be used to refine it. Figure 1b shows that the vertical component peak ground velocity from a local distance M5.4 event is linearly correlated with the teleseismic arrival delays. Additionally, as shown by Dolenc et al. (2005) the teleseismic arrival delay observations are well correlated with the depth to basement inferred from the USGS 3D velocity model (Figure 2). Here it is observed that delay time increases linearly with increasing basin thickness to about 3.5 km. For basin thicknesses greater than 3.5 km the arrival time and the microseism dominant period observations saturate suggesting that the effective seismic depth of the basins is 3.5 km. Although the basin defined from the gravity data (Jachens et al., 1999) shows maximum depths exceeding 6 km, the results of this analysis suggest that seismic velocities in the deepest parts of the basins are high enough to reduce the velocity discontinuity between the sedimentary strata and the basement.

The modeling of the teleseismic (Dolenc et al., 2005) and microseismic (Dolenc and Dreger, 2005) data indicate that the spatial extent of the basins in the USGS 3D model is superior to the coarse polygonal model of Stidham et al., (1999). Although the USGS model has slower velocities at the shallowest depths, we find that the arrival time delays and P-wave amplification are better modeled by the Stidham et al. (1999) model, which has slow velocities extending to greater depth.

We have developed a waveform inversion method to invert the teleseismic wavefield for the internal velocity structure of the basin. We assumed the basin geometry from the USGS V2 3D model (Brocher et al., 1997; Jachens et al., 1997), and inverted for the P (Vp) and S (Vs) velocity gradients within the basins. We assumed that the density scaled with Vp from the Nafe-Drake equation in Brocher et al. (2005). Figure 3a shows the fit to the data, and 3b the velocity models. The velocity gradient for the USGS 3D model is for the station 238 site. At this site the basin extends to a depth of 4km. The basin influence is clearly seen in terms of the higher amplitudes and waveform complexity at stations 120 and 238. In contrast the records at 186 (reference site outside the basin) and PG2 (over a bedrock ridge between the two Santa Clara Valley basins) are dominated by direct P and pP with relatively minor levels of coda. In Figure 3a the top row compares the observations (dotted) and synthetics (solid) for the USGS V2 3D model. The second row compares observations (dotted) and synthetics (solid) for the initial inversion model, which assumes a single velocity gradient structure within the basins. The basin geometry from the USGS V2 model was assumed. The third row compares the observed (dotted) and synthetic (solid) waveforms from the 3rd iteration of the inversion. The final model improves the timing of direct P, and also the waveforms for the direct P and pP phases, as well as the basin generated

arrivals located between P and pP (e.g Dolenc et al., 2005), and the later coda. The final model (Figure 3b) has significantly lower velocities over a larger depth section of the basin. In our ongoing work we will utilize the basin geometry of the version 3 (SF06) USGS 3D model (Brocher, 2005; Brocher et al., 2006; Jachens et al., 2006), as well as an inversion parameterization that allows more than one velocity gradient with depth to better match the structure present in the USGS 3D models.

Conclusions

We found strong basin signatures in teleseismic P-waveforms, and microseismic noise data obtained from the SCVSE. These metrics were found to linearly correlate, and also correlate with the peak ground velocity recorded for a local M5.4 event. The strong relationship between these three data sets indicates that they are sensitive to the same basin structure, and that they may be used to update the 3D basin structure in the Santa Clara Valley.

We have performed waveform inversions of the teleseismic wavefield and have found that relatively slow Santa Clara Valley basin velocities are needed to fit the time residuals as well as the waveforms. Our ongoing work will utilize the SF06 3D model as a starting point in the inversion. We will explore the ability of single and multiple gradient models in explaining the observations. Future work will also integrate the microseism and local earthquake waveform data in the inversion process.

References

Brocher, T. E., E. E. Brabb, R. D. Catchings, G. S. Fuis, T. E. Fumal, R. C. Jachens, A. S. Jayko, R. E. Kayen, R. J. McLaughlin, T. Parsons, M. J. Rymer, R. G. Stanley, and C. M. Wentworth (1997). A crustal-scale 3-D seismic velocity model for the San Francisco Bay area, California, *EOS Trans. AGU*, 78, F435.

Brocher, T. M. (2005). Empirical relations between elastic wavespeed and density in the Earth's crust, *Bull. Seism. Soc. Am.*, 95, 2093-2114.

Brocher, T., B. Aagaard, R. Simpson, and R. Jachens (2006). The new USGS 3D seismic velocity model for northern California: *Seism. Res. Lett.*,, v. 77, p. 271.

Dolenc, D., and D. Dreger (2005). Microseisms observations in the Santa Clara Valley, California, *Bull. Seism. Soc. Am.*, *95*(3), 1137-1149.

.

Dolenc, D., D. Dreger, and S. Larsen (2005). Basin structure influences on the propagation of teleseismic waves in the Santa Clara Valley, California, *Bull. Seism. Soc. Am.*, *95*(3), 1120-1136, 2005.

Dolenc, D., D. Dreger, and S. Larsen (2007). Simultaneous inversion of teleseismic, local, and microseism observations for the velocity structure within the Santa Clara Valley basins, *Seism. Res. Lett*., abstract, 2007 Annual SSA Meeting.

Jachens, R. C., R. F. Sikora, E. E. Brabb, C. M. Wentworth, T. M. Brocher, M. S. Marlow, and C. W. Roberts (1997). The basement interface: San Francisco Bay Area, California, 3-D seismic velocity model, *EOS Trans. AGU*, 78, F436.

Jachens, R., R. Simpson, R. Graymer, C. Wentworth, and T. Brocher (2006). Three-dimensional geologic map of Northern and Central California: A basin model for supporting earthquake simulations and other predictive modeling, *Seism. Res. Lett.*, v. 77, p. 270.

Lindh, A. G., J. P. Eaton, M. O. Allen, J. H. Healy, S. W. Stewart, and L. Damerell (1999). Calibration formulae and values for velocity seismometers used in the 1998 Santa Clara Valley, California, seismic experiment, *U.S. Geol. Surv. Open-File Rept. 99-434.*

Stidham, C., M. Antolik, D. Dreger, S. Larsen, and B. Romanowicz (1999). Three-Dimensional Structure Influences on the Strong Motion Wavefield of the 1989 Loma Prieta Earthquake, *Bull. Seism. Soc. Am.*, 89, 1184-1202.

Figures

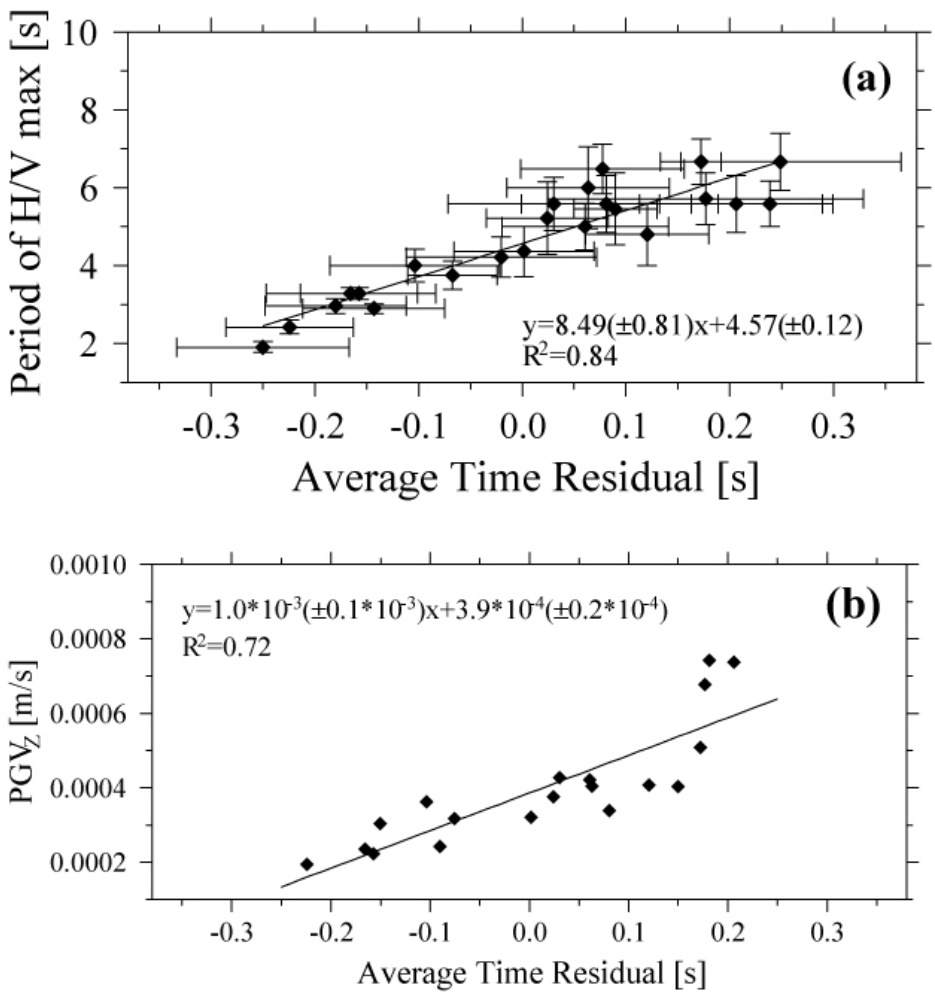

Figure 1 a) shows the correlation between the dominant period of the horizontal to vertical (H/V) spectral ratio with the residual P-wave arrival time averaged from the observations from 7 teleseisms. The error bars show the uncertainty in both the residual time and period estimates.

The correlation is remarkably linear. b) The vertical component peak ground velocity (PGV) is compared to the teleseismic P-wave time residuals. Again, there is a remarkably linear correlation between these two measures.

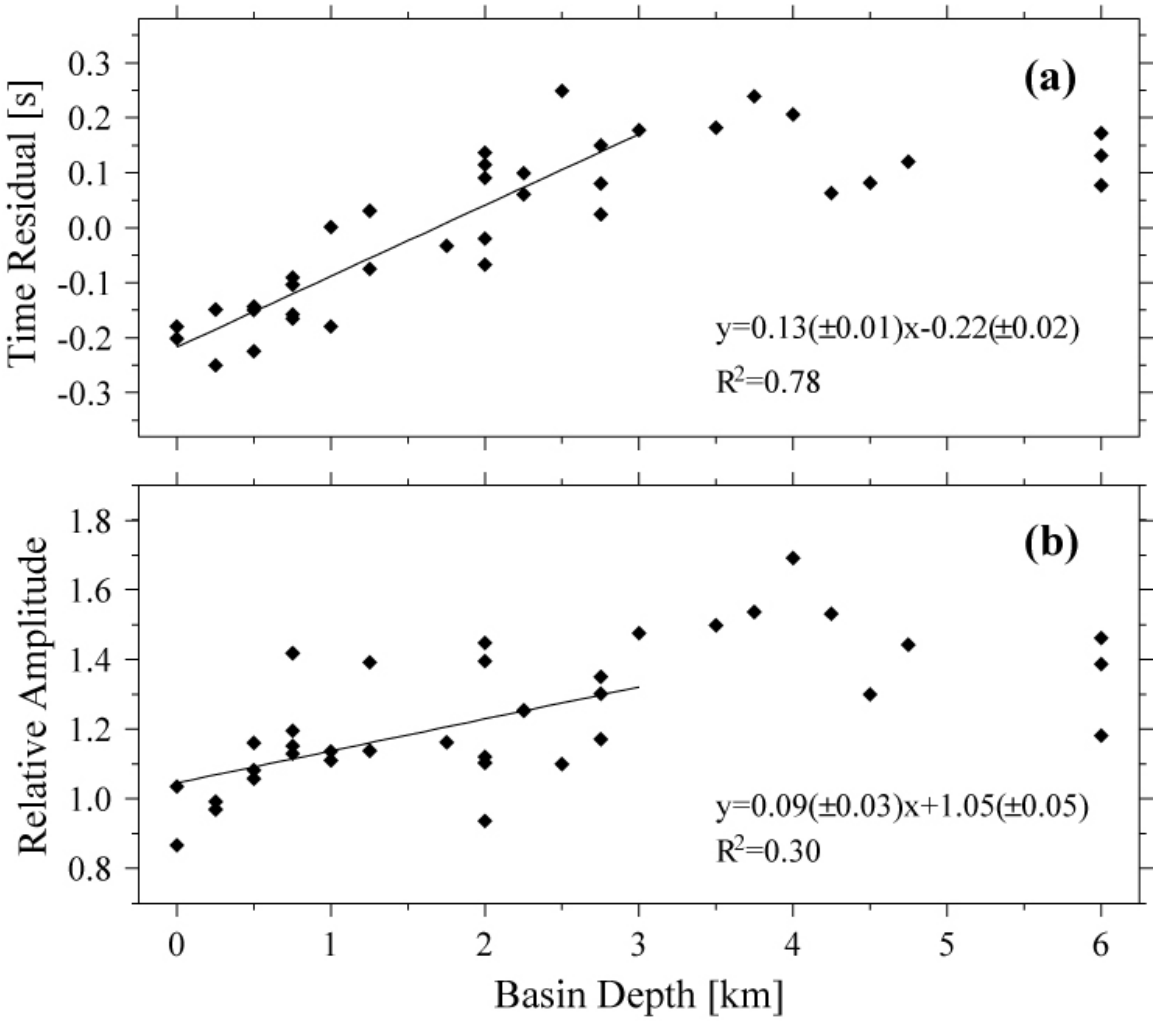

Figure 2. a) The teleseismic time residuals are compared to the basin depth in the USGS 3D model. The line was fit to a maximum depth of 3 km where there is a break in the relationship and the time residuals saturate. b) The relative amplitude of the teleseismic P-wave is plotted against basin depth. The amplitude increases with basin depth to about 3 km where it is also observed to saturate.

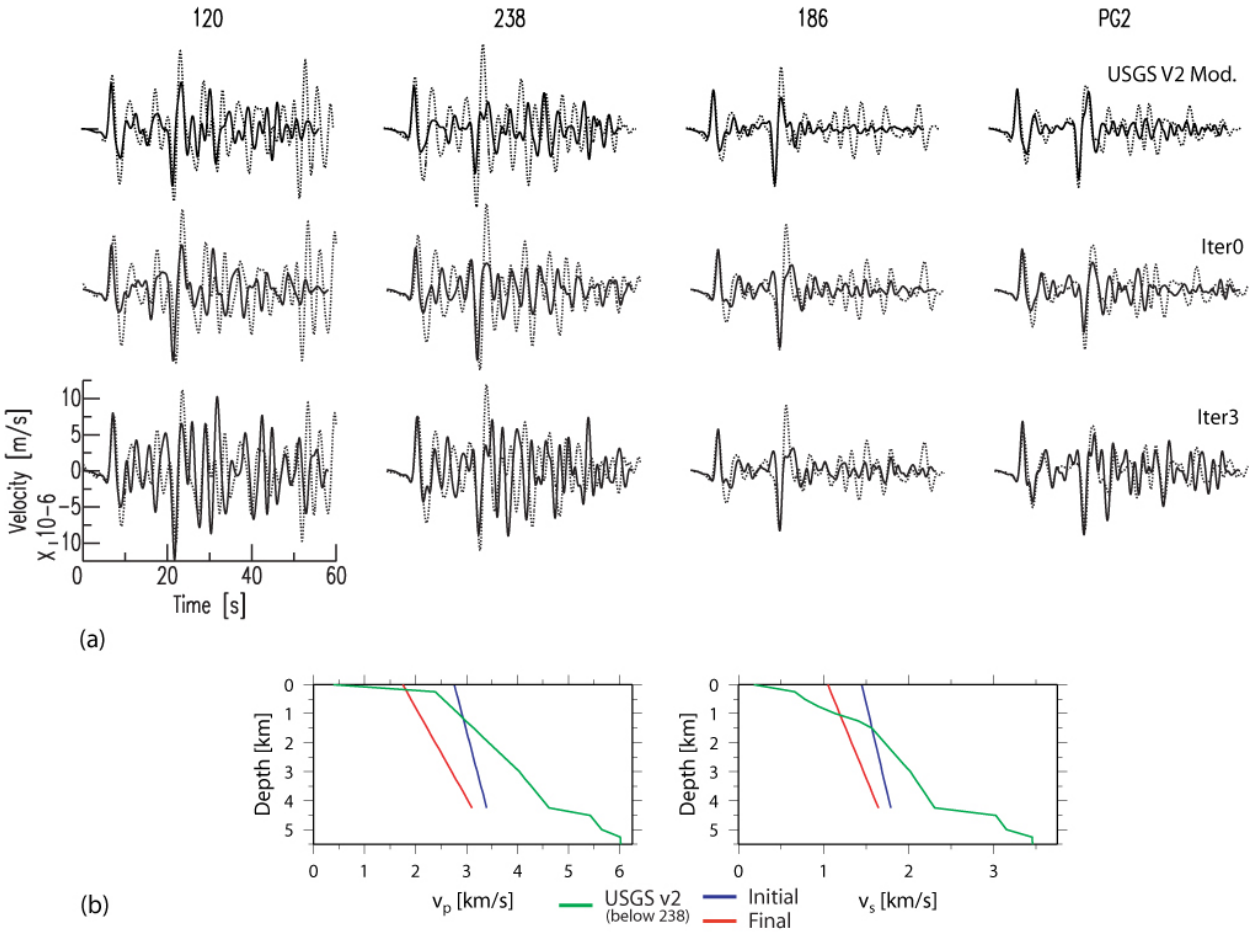

Figure 3. a) The observed (dotted) and predicted (solid) teleseismic P-waveforms are compared for the USGS V2 model, the initial inversion model (iter0) and the third iteration (iter3). The relatively simple waveform at station 186 is dominated by P and pP. The fit at the two basin sites (120 and 186) is greatly improved with the updated model. b) The velocity gradient from the USGS model (Green) is compared to the initial model (blue) and the model obtained after three iterations (red). In this initial case we assumed a single velocity gradient within the basin structure. Future work will consider several gradient layers to more closely approximate the USGS model as a starting point in the inversion.

Appendix

Bulletin of the Seismological Society of America, Vol. 95, No. 3, pp. 1120–1136, June 2005, doi: 10.1785/0120040059

Basin Structure Influences on the Propagation of Teleseismic Waves in the Santa Clara Valley, California

by David Dolenc, Doug Dreger, and Shawn Larsen

Abstract We have investigated ground-motion amplification in the Santa Clara Valley (SCV) using teleseismic *P* waves observed during the 1998 deployment of 41 short-period seismometers. The Santa Clara Valley Seismic Experiment (SCVSE) (Lindh *et al.*, 1999; Fletcher *et al.*, 2003) recorded many local and regional earthquakes and seven large ($M_w > 6.4$) teleseisms. Measured teleseismic *P*-wave arrival-time delays, relative *P*-wave amplification, and *P*-wave energy were used in the analysis. The relative *P*-wave amplification is found to correlate strongly with the arrival-time delays. In addition, the *P*-wave energy is found to correlate with the observed teleseismic delays. We also compared observed *P*-wave arrival-time delays and *P*-wave amplification with synthetics computed by using 3D finite-difference simulations of the teleseismic wave field to model these parameters using both the University of California, Berkeley (UCB) (Stidham *et al.*, 1999; Stidham, 1999) and the U.S. Geological Survey (USGS) (Brocher *et al.*, 1997; Jachens *et al.*, 1997) 3D velocity models. The results indicate that arrival-time delays on the order of ± 0.25 sec correlate strongly with the reported basin depths in the two models. We find that the correlation between the arrival-time delays and basin depth is strongest for the USGS model. However, the UCB velocity model yields wave amplification that better matches the data. The finite-difference simulations indicate that, in general, the observations may be reproduced by either of the 3D velocity models, although refinements to the proposed 3D structure for the SCV are needed.

Introduction

The Santa Clara Valley (SCV) is an alluvial basin located south of the San Francisco Bay. It includes two elongated basins, the Cupertino basin in the west and the Evergreen basin in the east. The sediments overlaying the Franciscan basement are mainly Pliocene to Quaternary alluvial gravels and sands (Wentworth *et al.*, 1997). The proximity of the SCV to the active San Andreas, Hayward, Calaveras, Sargent, and Rodgers Creek faults, and its location beneath the heavily populated San Jose metropolitan area, have resulted in an increased interest to better delineate the SCV structure. Several studies have focused on the hazard associated with the two elongated and possibly deep basins. Studies by Frankel and Vidale (1992), Stidham *et al.*, (1999), Stidham (1999), Frankel *et al.*, (2001), Hartzell *et al.*, (2001), and Fletcher *et al.*, (2003) are all examples of these efforts. Using a 3D velocity model of the region, Stidham *et al.* (1999) successfully modeled the strong-motion wave field of the 1989 Loma Prieta earthquake. However, one of the concerns raised by the study was the limited sampling of sites located over the SCV. Stidham (1999), in her thesis work, examined several 3D velocity models in the simulation of small to moderate local earthquakes. These studies demonstrated the sensitivity of the synthetic seismograms to basin heterogeneity, to the velocity contrasts across the major strike-slip faults of the region, and to the deep crustal structure.

To address some of these concerns, the Santa Clara Valley Seismic Experiment (SCVSE) was carried out by the U.S. Geological Survey (USGS), University of California, Berkeley (UCB), and Incorporated Research Institutions for Seismology Program for Array Seismic Studies of Continental Lithosphere (IRIS PASSCAL). In the experiment, 41 seismic stations were deployed across the SCV from June through November 1998 (Fig. 1a). The array recorded a number of local, regional and teleseismic earthquakes. Seven of the teleseismic events (Table 1, Fig. 1b) had high signal-to-noise levels, allowing detailed analysis.

Teleseismic waves are well suited to investigating 3D details of a local velocity structure as previous studies in the Salt Lake Basin (Olsen and Schuster, 1995; Olsen *et al.*, 1995) and observations in the Seattle basin (Pratt *et al.*, 2003) have shown. Because the distance from the event is large compared with the aperture of the array, the seismic wave field is essentially uniform as it arrives beneath the

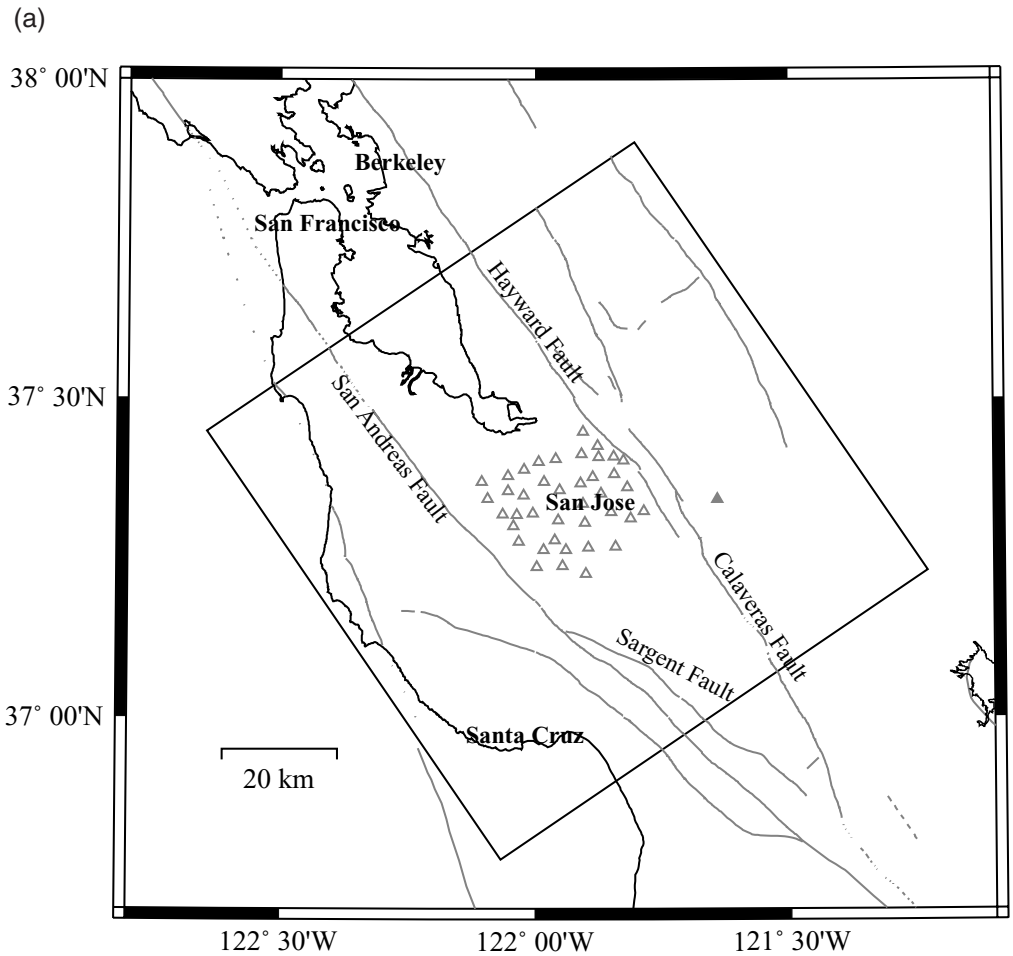

Figure 1. (a) Location of the temporary SCV seismic array south of the San Francisco Bay. Open triangles indicate SCVSE seismic stations, and the filled triangle indicates permanent station MHC of the Berkeley Digital Seismic Network. The box shows the size of the model used in the E3D finite-difference simulations. Gray lines are the active faults in the region. (b) Locations of the teleseismic events used in this study. (c) Closer look at the SCV region. Numbers indicate SCVSE seismic stations. Dashed lines denote the contours of the basins from the UCB model at the surface and at the 1-km depth. Contours of the basins from the USGS model at 1 km, 3 km, 5 km, and 6 km depth are shown in gray. The region of interest was divided into sections A, B, and C. The UCB and the USGS velocity model cross sections along lines A, B, and C are shown in Figure 4. (*continued*)

region of study. The source contributions and the near-source and mantle-travel paths are also essentially the same for all the SCV stations. We may therefore assume that the differences in the observed teleseismic waveforms are caused by differences in crustal structure beneath the recording array.

In this article we present results of analyses of teleseismic *P*-wave arrival-time delays, relative *P*-wave amplification, *P*-wave energy, seismic waveforms, and basin-converted arrivals with the objective of testing proposed 3D velocity models for the SCV region and to determine whether the teleseismic wave field can delineate 3D basin structure to use as a basis for improving velocity models.

Data Processing

The locations of the SCVSE seismic stations we use are shown in Figure 1c. The stations provided good coverage of the SCV. All the stations except station 160 were situated on SCV alluvium. Station 160, in the eastern part of the Evergreen basin, was placed on Mesozoic rocks. Station MHC, a permanent station of the Berkeley Digital Seismic Network (BDSN) located on hard Mesozoic rocks east of the SCV, was used in addition to SCVSE seismic stations as a reference hard-rock site. None of the SCVSE seismic stations were located in the San Francisco Bay mud.

Mark Products L-22D seismometers with 2-Hz natural frequency from the USGS and IRIS PASSCAL as well as

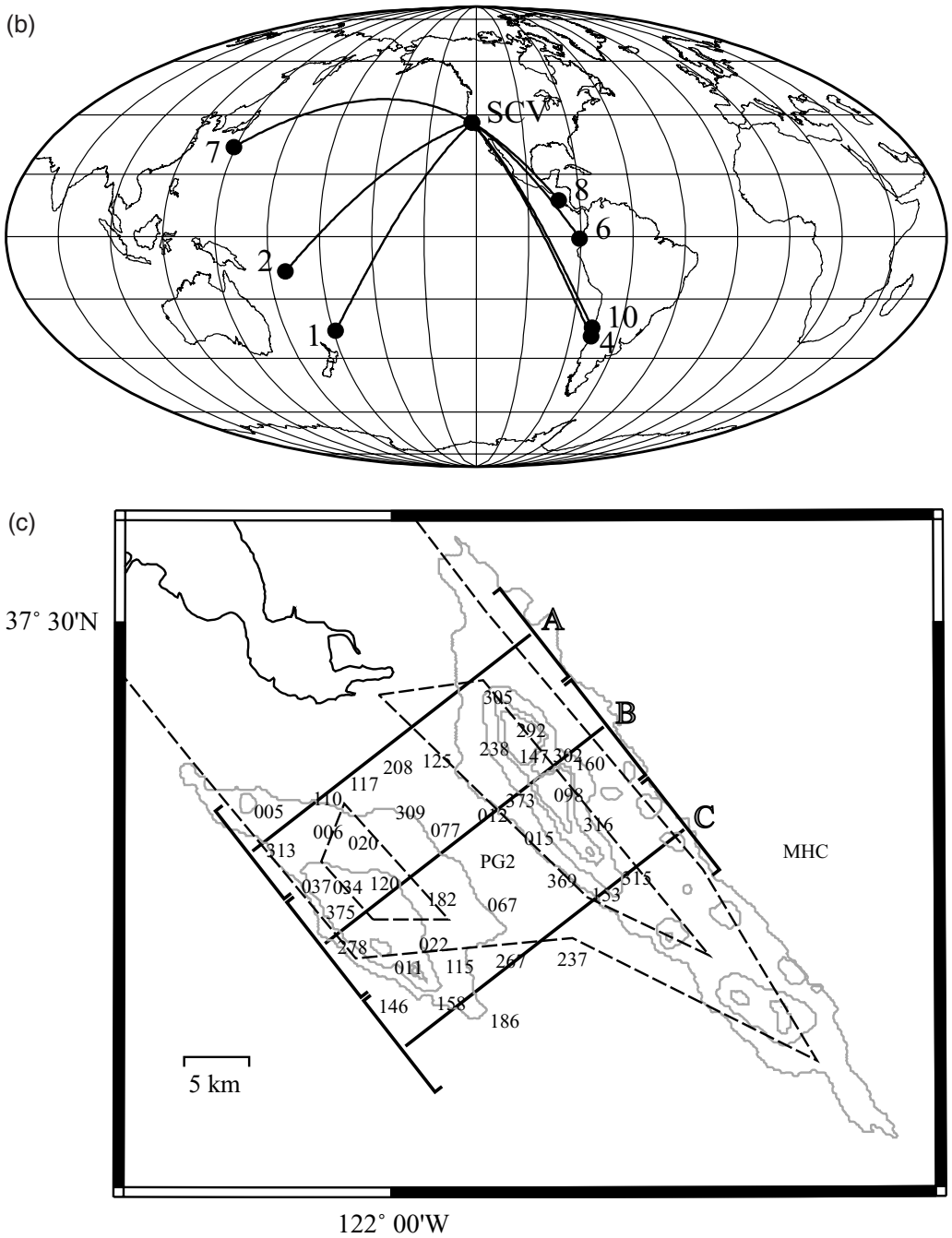

Figure 1. Continued

L-4C seismometers with 1-Hz natural frequency from the USGS were used together with three-channel 24-bit RefTek 72a-07s recorders. Global Positioning System (GPS) receivers were connected to the recorders to keep the internal clock accurate. Data were sampled continuously at 50 Hz. The USGS instruments had been individually calibrated and the measured parameters should be accurate to within $\pm 5\%$. For the PASSCAL instruments, nominal values were used, which were accurate to within 15% (Lindh *et al.*, 1999). For the analysis, the vertical-component ground-velocity records were processed by deconvolving the reported instrument-response parameters (Lindh *et al.*, 1999) and filtering between 0.1 and 0.5 Hz by using a four-pole acausal Butterworth bandpass filter. We found that the short-period instruments recorded the teleseismic *P* waves with excellent signal-to-noise ratios to a minimum frequency of 0.1 Hz. *S* waves were not well recorded because of the limited instrument response. The low-pass filter was applied to remove the higher frequency cultural noise from the urban environment.

Table 1
List of the Selected Teleseismic Events from the Harvard Moment Tensor Catalog

Event No.	Region	Latitude	Longitude	Date (mm/dd)	Time	M_w	Depth (km)
1	Kermadec Islands	−30.51	−178.71	07/09	14:45:49	6.9	154
2	Santa Cruz Islands	−10.91	166.09	07/16	11:56:42	7.0	100
4	Near Coast of Central Chile	−32.30	−71.67	07/29	07:14:29	6.4	58
6	Near Coast of Ecuador	−0.57	−80.48	08/04	18:59:29	7.1	26
7	Bonin Islands Region	28.99	139.47	08/20	06:41:10	7.1	426
8	Off Coast of Central America	11.58	−88.55	08/23	13:57:17	6.7	15
10	Near Coast of Central Chile	−29.56	−71.97	09/03	17:38:05	6.5	34

Observations

For a given event, the waveforms can differ greatly at the stations of the array. Figure 2 illustrates the differences in the amplification of the initial *P* wave and in the development of the *P*-wave coda at four sites. Station 120 was located over the Cupertino basin, station 238 over the deep part of the Evergreen basin, and station 186 south of the Cupertino basin (see Fig. 1c). In each case the record from station PG2, located on the bedrock ridge between the two SCV basins, is shown for comparison. The station 186 record is very similar to that of PG2. The amplitudes of their first *P*-wave arrivals are almost identical and they both lack the large-amplitude, extended coda wave field observed at stations 120 and 238.

For the analysis, we made measurements on the teleseismic data that included *P*-wave arrival times, amplitudes of the initial *P* waves, and *P*-wave energy. We first measured the relative *P*-wave arrival-time delays across the SCV in which arrival-time delays are with respect to a reference station assumed to be located outside the basins. Although essentially the same results were obtained by using stations MHC or 186 as a reference, in the following we use station 186 because it is one of the SCV array stations. *P*-wave amplitudes on station 186 were consistently small, the *P*-wave coda short, and both the UCB and USGS velocity models agree that it is located outside the SCV basins. Station 160 was an alternative candidate for a reference station, because it was the only SCV array station located on rock. We rejected it because the Evergreen basin extends to the east of it in both models.

The arrival times were determined by cross-correlating the first quarter-cycle of the initial *P* waveform. Nearly identical results were obtained using the first half-cycle, and very similar results were obtained when the entire *P* waveform was cross-correlated. A planar trend in arrival time was then fit to the data and removed, giving the travel-time residual for each station. The residuals for event 4 clearly outline the deep basins and intervening bedrock ridge (Fig. 3a). The range in the arrival-time delays is ± 0.25 sec, in which the positive delays correspond to later arriving *P* waves. The *P*-wave amplification with respect to station 186 also correlates with the SCV structure (Fig. 3b). The range in *P*-wave amplification is found to be from 0.8 to approximately 1.5 with respect to station 186. Similar results were obtained for all seven events.

UCB and USGS Version 2 Velocity and Density Models

The UCB and the USGS models cover the area from the latitude of Monterey, California, to just north of San Pablo Bay, and from the Pacific coast to the Great Valley in the east. The USGS model has *P*- and *S*-wave velocity and density defined at each point within the model, and the UCB model has the three variables parameterized. Figure 4 shows cross sections of the two models along the lines A, B, and C indicated in Figure 1c.

The UCB model (Stidham, 1999; Stidham *et al.*, 1999) was created as a simple model that incorporates the main geologic blocks present in the wider San Francisco Bay area. In addition to shallow alluvial basins, it includes velocity contrasts across the strike-slip faults. The bedrock consists of layers that vary with depth in the upper crust and are homogeneous below a midcrustal discontinuity located at 17 km depth (Jachens *et al.*, 1995). The depth of the midcrustal reflector and of the Moho were taken from the BASIX study (Brocher *et al.*, 1994) and from broadband waveform modeling (Dreger and Romanowicz, 1994). The extent of alluvium in the model was determined from seismic reflection studies and from the borehole and gravity surveys. In the SCV region, depth to the bedrock was determined mainly by the interpretation of gravity anomalies. The slowest shear-wave velocity in the model is 1 km/sec and the model does not include topography.

The USGS model used in this study is the second revision of the San Francisco Bay area 3D velocity model (Brocher *et al.*, 1997; Jachens *et al.*, 1997) developed by Jachens and others at the USGS from a careful conversion of known geology into seismic velocity and density. The model extends to 28.5 km depth and includes the mafic lower crust and the mantle. It was constructed by using surface geology, gravity inversion data, seismic refraction data, and borehole logs. It also does not include topography. Although the basins may extend deeper than 6 km, the authors as-

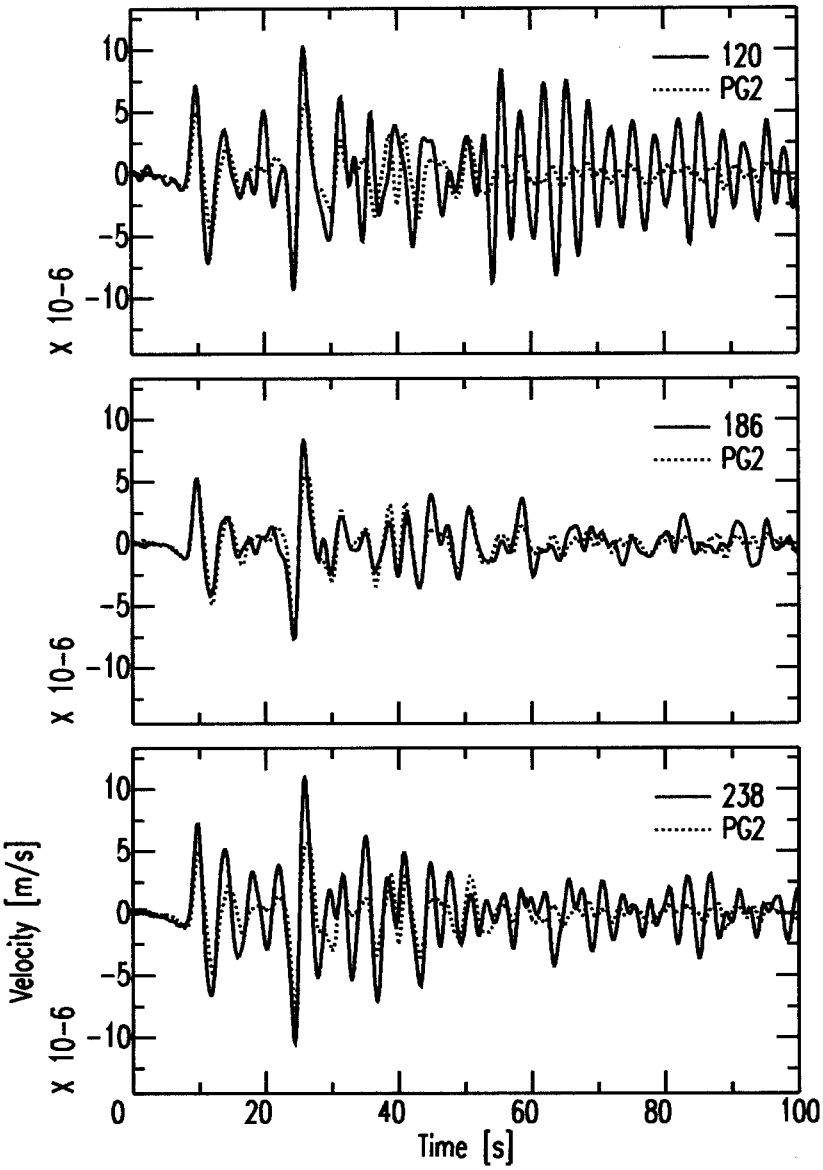

Figure 2. Vertical velocity seismograms for event 4 recorded on SCV stations 120, 186, and 238. Also shown in all three panels is station PG2 (dotted). The first arrival is a *P* wave followed by a *pP* wave about 15 sec later. See Figure 1c for station locations.

sumed that below this depth the seismic velocities are indistinguishable from those of the basement. Version 2 of the model incorporates velocity contrasts across the faults. The model grid spacing in the upper 625 m is 125 m. At intermediate depths, down to 6 km, the grid spacing is 250 m. From there to the deepest extent of the model, 28.5 km, grid points are 500 m apart. The slowest shear-wave velocity in the model is 83 m/sec.

The basin depths in the UCB model are well defined contrasts between the uniform basin velocities and the faster bedrock (Fig. 4). The basin depths for the USGS model were determined by comparing the velocity and density of the vertical profile at each site with the vertical profile of a non-basin site. The depth at which there is no difference in *P*- and *S*-wave velocity and density was taken as the basin depth.

The UCB and the USGS model cross sections are shown in Figure 4. The structure around and under the basins is similar in both models and they both have bedrock velocity gradients. The deep structure in the two models is also very similar.

Some of the more important differences between the two models are as follows. The UCB model has uniform *P*- and *S*-wave velocities (1.75 and 1 km/sec), and density (2 g/cm^3) within the basins. The USGS model has basin velocities and density that increase with depth. In the UCB model the maximum basin depth is 2 km in the eastern and 1.5 km in the western basin. In the USGS model the maximum basin depth is 6.5 km in the eastern and 4.5 km in the western basin. Although the basins in the USGS model are much deeper, the regions with slow velocities are shallow and their depths are similar to the UCB model. The deepest grid layer in the USGS model that includes *S*-wave velocities slower or equal to 1 km/sec, is at 1.5 km depth. By this measure, the

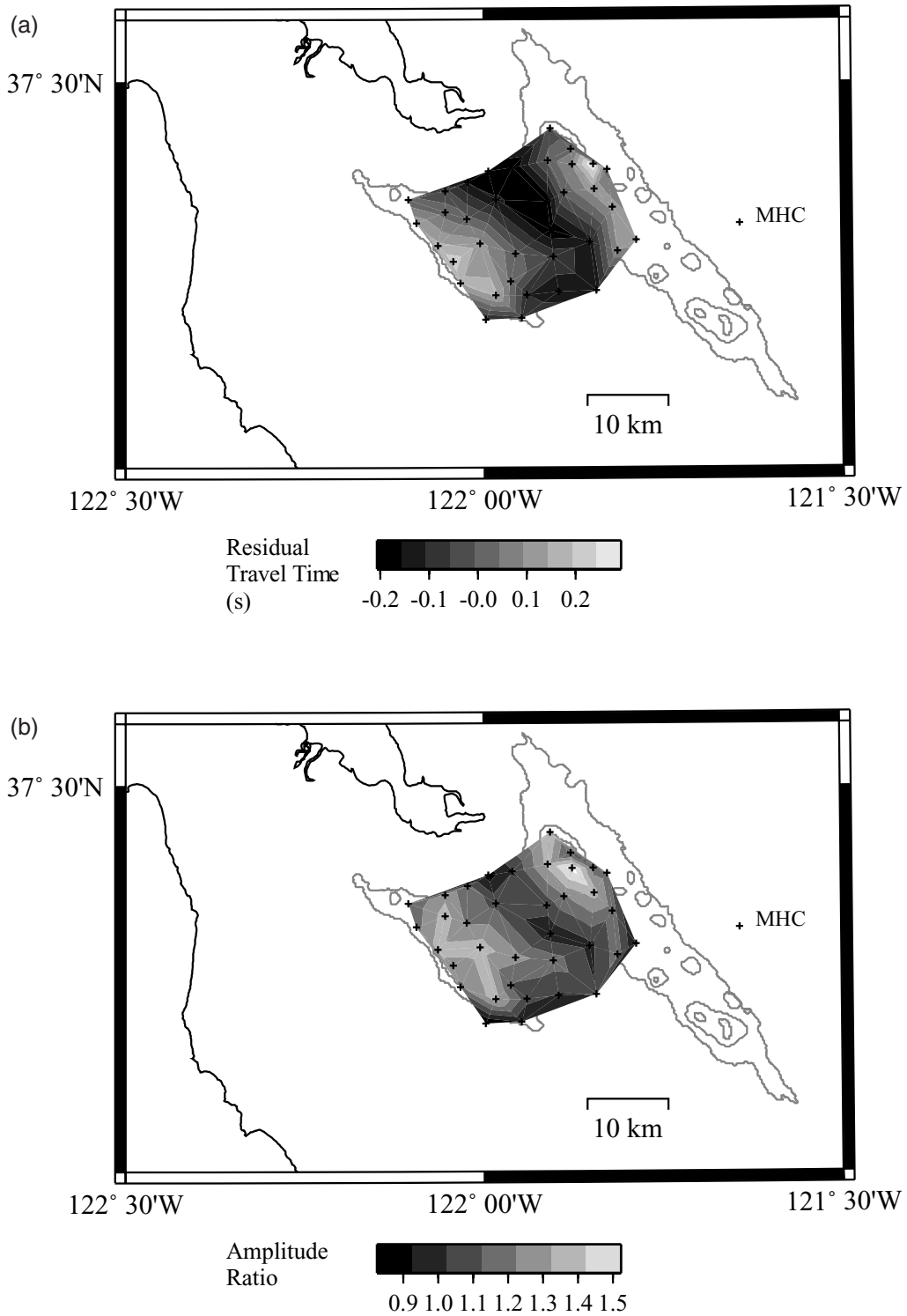

Figure 3. (a) Observed *P*-wave residuals for the event 4. (b) Observed *P*-wave amplitudes for the event 4 relative to reference station 186. Station 186 was located south of the Cupertino basin (see Fig. 1c). Contours of the basins from the USGS model at 1 km, 3 km, 5 km, and 6 km depth are shown in gray.

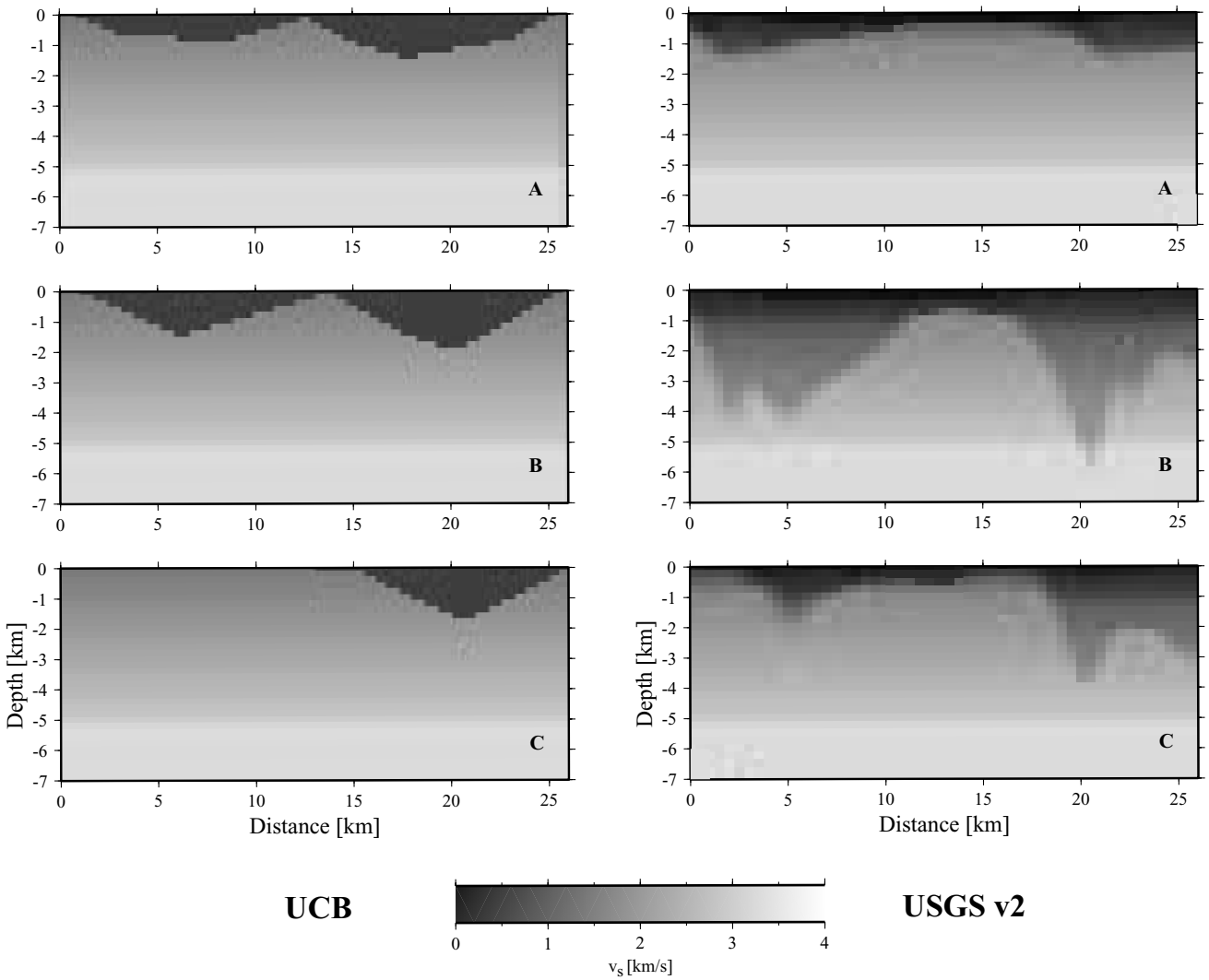

Figure 4. Cross sections of shear-wave velocities from the UCB and the USGS models across the SCV basins, along the lines A, B, and C shown in Figure 1c.

basins in the USGS model are shallower than in the UCB model. In the UCB model the two basins have a very simple geometry. In the USGS model the two basins have an irregular shape, which is a result of the gravity inversion mapped into the model. In the UCB model the western basin does not extend as far south as it does in the USGS model, and in the UCB model the Cupertino and Evergreen basins are not as wide as in the USGS model.

The UCB model was designed for use with the E3D finite-difference code (Stidham *et al.*, 1999) and no changes were made to the model for the purpose of this study. Before the USGS model was used with the finite-difference code, the top section of the model was resampled and the bottom section of the model was interpolated to a uniform 250-m grid spacing. Because the surface layer was not yet available when we began our study, the layer at 125 m was used as the surface layer. Because of computational limitations, the slowest velocities in the model were increased to a minimum *S*-wave velocity of 1 km/sec. The slowest *P*-wave velocity was 1.75 km/sec. The velocity increases affected the model down to 1.5 km depth. A high-resolution run was also performed in which the grid spacing was 125 m and the slowest *P*- and *S*-wave velocities were 0.9 and 0.52 km/sec, respectively, affecting the model to a depth of 250 m.

Modeling

Although a ray approach could be used efficiently for the purpose of estimating arrival-time delays and *P*-wave amplitudes, we used an elastic finite-difference technique to calculate synthetic waveforms because of our interest in modeling converted arrivals, which are seen to contribute significantly to the observed seismic waveforms (see Fig. 2).

The elastic finite-difference code E3D (Larsen and Schultz, 1995) used in this study is accurate to the fourth order in space and to the second order in time. It utilizes a

regularly spaced grid that is staggered in both space and time for the six-component stress and three-component velocity fields. Stress-free surface conditions and absorbing boundary conditions (Clayton and Engquist, 1977) were used, and a "sponge" boundary layer (Cerjan *et al.*, 1985) was applied to minimize reflections from the model boundaries. Attenuation and topography were not included in the modeling.

Most of the modeling was performed by using a 250-m grid spacing and a minimum shear-wave velocity of 1 km/sec. At five grid points per wavelength, frequencies up to 0.8 Hz were simulated with minimal grid-dispersion effects (Levander, 1988). In our analysis we compared simulations and observations in the 0.1- to 0.5-Hz passband. At 0.5 Hz maximum frequency there are eight grid points per wavelength giving greater accuracy. We performed a high-resolution run in which the grid spacing was reduced to 125 m, giving 16 grid points per wavelength at 0.5-Hz maximum frequency. The synthetics from the 250-m and 125-m grid runs were nearly identical in 0.1- to 0.5-Hz passband.

The size of the largest model was $115 \times 115 \times 80$ km with more than 67.0×10^6 grid points. Each simulation required approximately 3.5 GB of memory. To examine the importance of the slow velocities defined in the USGS model, we calculated a few high-resolution simulations with 125-m grid spacing and minimum *P*- and *S*-wave velocities of 900 and 520 m/sec. The model for the high-resolution runs had more than 536.0×10^6 grid points and required approximately 28 GB of memory.

Most of the computations were performed on the vector parallel supercomputer Fujitsu VPP700E (32 processors, 64-GB memory) at the Institute of Physical and Chemical Research (RIKEN) in Japan. A typical run using a 250-m grid spacing was completed in 1 hr. Smaller models and shorter test runs were calculated on a Sun Enterprise 3000 computer (3 processors, 4.75-GB memory) at the Berkeley Seismological Laboratory.

To model the plane wave from the teleseismic events, we used a disc of point sources spaced 1.25 km apart in the deepest homogeneous layer of the velocity model, representing the upper mantle. The time history for each compressional point source had a Gaussian pulse shape. For each event the disc was oriented in space to have the backazimuth and incident angle of the incoming *P* wave. By modeling the plane orientation with a horizontal layer of sources delayed in time, we were able to decrease the model depth to 40 km, reducing memory requirements and calculation time. Although the boundaries were absorbing, they still reflected some energy, resulting in undesirable late arrivals, mainly because some of the sources used to simulate the plane wave were close to the model boundaries. In the modeling, care was taken to reduce late arrivals by increasing the model dimensions, tapering the point sources, and using a few grid-point thick "sponge" boundary layer (Cerjan *et al.*, 1985). The maximum amplitudes of the late arrivals that were due to the finite model dimensions and the finiteness of the approximated plane wave were estimated by simulations using a homogeneous model of the same dimensions and were found to be less than 15% of the first pulse (Fig. 5).

Results

P-wave Arrival Delays, Amplification, and Energy

All seven teleseismic events were forward modeled with the E3D code with both the UCB and the USGS models. The measured travel-time residuals and relative amplitudes at all stations show only small variations between the individual events, leading to the conclusion that the orientation of the incoming plane wave has little influence on basin response. The results for both the observed and the simulated travel-time residuals averaged over all events are presented in Figure 6a, where panels A, B, and C correspond to the sections indicated in Figure 1c. The measurements made on the synthetics were obtained in the same manner as in the observations. The mean values and standard deviations using the seven events are given for each station as a function of the distance across the SCV. The results for the observed and simulated amplitude analyses are presented in Figure 6b. The observations show that average amplitude on station 238, located over the Evergreen basin, is 46% larger than the observed amplitude at station PG2 that was located between the two basins. Average amplitude at station 120, located over the Cupertino basin, is 54% larger than at station PG2.

The sinusoidal signal across the basins and basement ridge is observed in both the data and the synthetics, for travel-time residuals as well as amplitudes. However, the observed data (gray) has larger variance than the synthetics. This means that parameters other than angle of incidence and azimuth have a significant impact on site response. This might be caused by the large-scale structure in the lower crust or Moho or by unknown point scatterers in the actual earth.

On the one hand, the UCB model matches the observations better because it has larger overall variation and range in the amplitudes and travel-time residuals. On the other hand, the shape of the observed time residuals in the northeast and the southwest corners of cross section B is better captured by the USGS model (see Fig. 6a, panel B). This indicates that the Evergreen and the Cupertino basin may be wider than currently modeled in the UCB model. The USGS model matches better the width of the negative time residuals presented in the middle part of cross section B, suggesting that the ridge between the two basins is wider than assumed by the UCB model. The variations in time residuals in the southwest edge of cross section C are better matched by the USGS model, in which the Cupertino basin extends further to the south than in the UCB model.

The average time residuals for all of the teleseismic events as a function of basin depth in the USGS and the UCB model are presented in Figure 7a,b. For both models positive delays correlate with greater basin depth. The USGS model

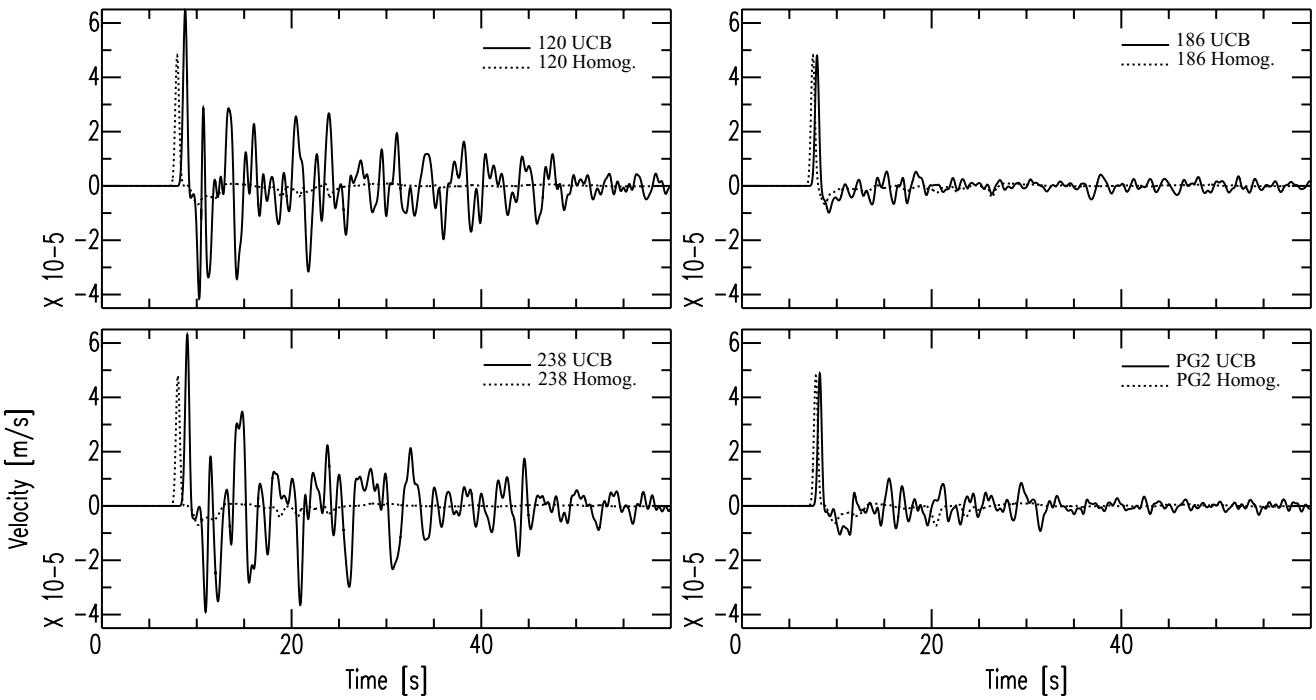

Figure 5. Synthetic waveforms for the UCB (solid) and for the homogeneous model (dotted) for the *P* wave of the event 4 on stations 120, 238, 186, and PG2. Late arrivals in the homogeneous model are due to the finite-model dimensions and finite-plane wave approximation.

with a more detailed basin geometry produces a more systematic and superior correlation of basin depth and *P*-wave arrival-time delay. The time residuals for the USGS model increase with increasing basin depth until about 2 km depth. Then, as the depth increases, the travel-time residuals remain more or less the same. This indicates that the slow velocities in the shallow layers contribute most to the delay. Although the basins are deep, the velocity at depth is very similar to that of the neighboring bedrock, so it has little influence on the travel time. For the UCB model the scatter is much larger, which is likely because of the relatively coarse structure of the model, but a correlation with depth can still be observed as the data and synthetics for the stations located above the basin deeper than 0.8 km show an increase in the travel-times residuals (Fig. 7b).

The relative amplification for the seven events as a function of basin depth in the USGS and the UCB model is presented in Figure 7c, d. In this case, the general trend with greater basin depth is not as clear as it was for the travel-time residuals. The correlation between the modeled *P*-wave amplitude and basin depth for the UCB model is seen to be good for depths less than 600 m, and for greater depths the average amplification is seen to be flat. For the USGS model the range of the modeled *P*-wave amplifications is much smaller, as already seen in Figure 6b. The correlation between the modeled *P*-wave amplitude and the USGS model basin depth can be seen for depths less than 1.8 km, but is much less pronounced than for the UCB model. This is because of continuous reduction in velocity throughout the basins in the USGS model. The UCB model, on the other hand, has a strong impedance contrast between the basin and the basement.

To investigate the importance of the slow velocities in the USGS model, we performed a few high-resolution runs with 125-m grid spacing and minimum *P*- and *S*-wave velocities of 900 and 520 m/sec (Dolenc, 2001). This changed the travel-time residuals only slightly (average change was 0.01 sec), because the inclusion of slower velocities affected only the top three grid points. In general, the relative amplitudes increased; however, the increased amplification did not account for the observations (average change was 2.4%). This indicates that the peak values, measured at relatively long periods ($T \geq 2$ sec), are largely unaffected by the very slow shallow structure and that to the first order they are sensitive to the basin/basement impedance contrast and the basin geometry.

Judging by results from the study of travel-time residuals the spatial extent and basin geometry of the USGS model is superior. However, a comparison of the relative amplitude shows that the USGS model does not explain the range of observed amplifications. The UCB model seems to explain the relative *P*-wave amplification reasonably well. The relative amplification increases from zero to 600 m basin depth, at which point it is fairly constant (see results for UCB model in Fig. 7d). This is expected because the basins in the UCB model have a constant velocity and the basin/basement im-

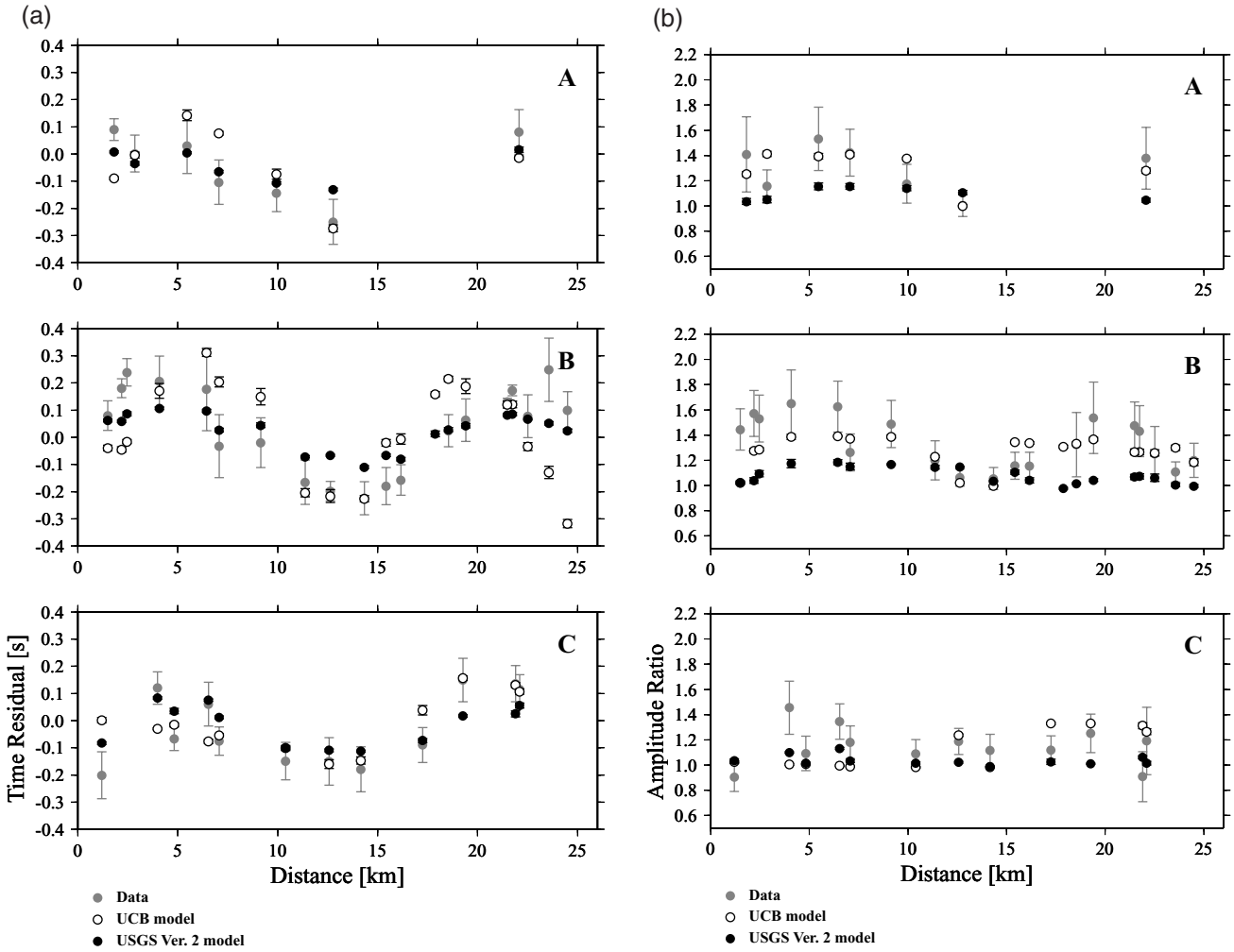

Figure 6. (a) Travel-time residuals for the observed and simulated waveforms across the profiles A, B, and C shown in Figure 1c. The mean values and standard deviations for the seven teleseismic events are shown. (b) Relative amplitudes for the observed and simulated waveforms. Presented values are relative to station 186, located south of the Cupertino basin (see Fig. 1c). The mean values and standard deviations for the seven teleseismic events are shown. Waveforms have been bandpass filtered between 0.1 and 0.5 Hz.

pedance is therefore also fairly constant. Thus the increase in amplification for small basin depths (< 600 m) must be a basin edge effect. Over the deepest parts of the basin, the amplification is caused entirely by the basin/basement impedance contrast because there is no internal amplification in the basin. Finally, the spatial correlation of time residuals agrees better with the USGS model, and, therefore, revisions to the SCV velocity model should start with the basin geometry specified in the USGS model, with perhaps a less pronounced internal basin velocity gradient.

To measure the energy of the incoming *P* wave, we squared and integrated 120 sec of the vertical waveforms after the *P*-wave arrival at each station. Figure 8 shows the ratio of the *P*-wave energy at each station to that at station 186, averaged over all seven teleseismic events. The correlation between the increased wave energy and the outline of the Cupertino and the Evergreen basin in the USGS model is excellent. The intervening bedrock ridge also shows up prominently with lower levels of *P*-wave energy. The average for the seven events is shown because no systematic variation in *P*-wave energy with respect to event backazimuth and incident angle of the primary *P* wave was observed (Dolenc, 2001). Station 238, located over the Evergreen basin, shows a 228% increase in energy relative to station PG2 that was located between the two basins. Station 120, located over the Cupertino basin, shows a 267% increase in energy relative to station PG2.

Figure 9 compares the USGS basin depth, UCB basin depth, *P*-wave amplification, and *P*-wave energy, all as functions of the observed teleseismic *P*-wave arrival-time delay. The bottom two panels in Figure 9 compare just the observations and do not use any information from the two models.

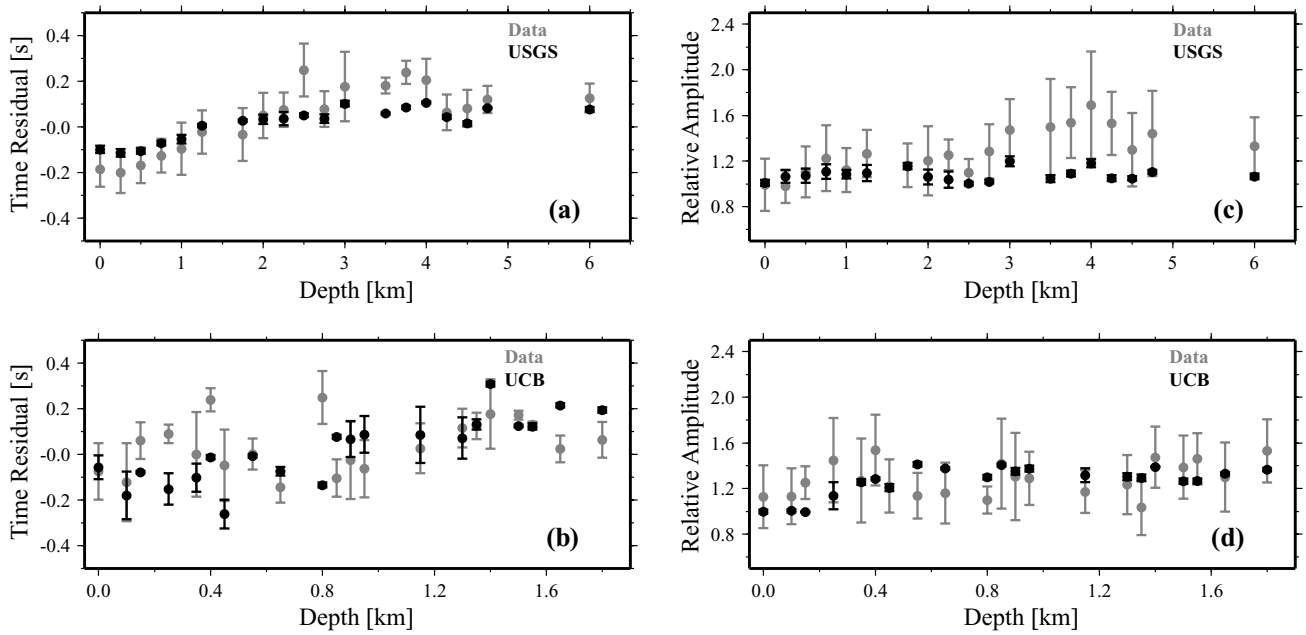

Figure 7. Travel-time residuals averaged over all events as a function of basin depth for the observed (gray) and synthetic (black) data for the USGS (a) and the UCB models (b). Also shown are the relative amplitudes averaged over all events for the observed (gray) and synthetic (black) data for the USGS (c) and the UCB models (d). In addition, the results for all stations with the same basin depth were averaged; therefore, only one value is presented for each depth.

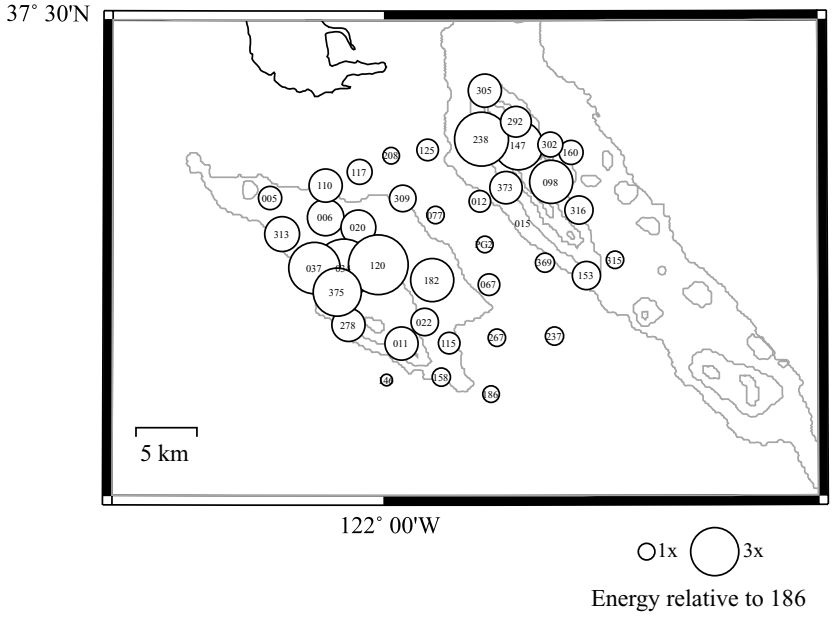

Figure 8. The average *P*-wave energy for the seven teleseismic events relative to station 186. Contours of the basins from the USGS model at 1 km, 3 km, 5 km, and 6 km depth are shown in gray.

For the teleseismic observations the results for the seven events were averaged. The basin uncertainty is shown as 20% of the basin depth. This value is given for the USGS model (Jachens *et al.*, 1997) and is used for the UCB model. Figure 9 demonstrates the correlation of all the observables with respect to the reported basin depth, which suggests that the teleseismic observations may be used to refine basin structure. It also suggests that it may be possible to deduce site amplification characteristics that are applicable to local earthquake basin excitation from the observed teleseismic arrival-time delay and relative amplitude.

The correlations also allow for regressions to obtain equations to predict time residuals, relative amplitudes, and relative *P*-wave energy. Figure 10 shows the observed val-

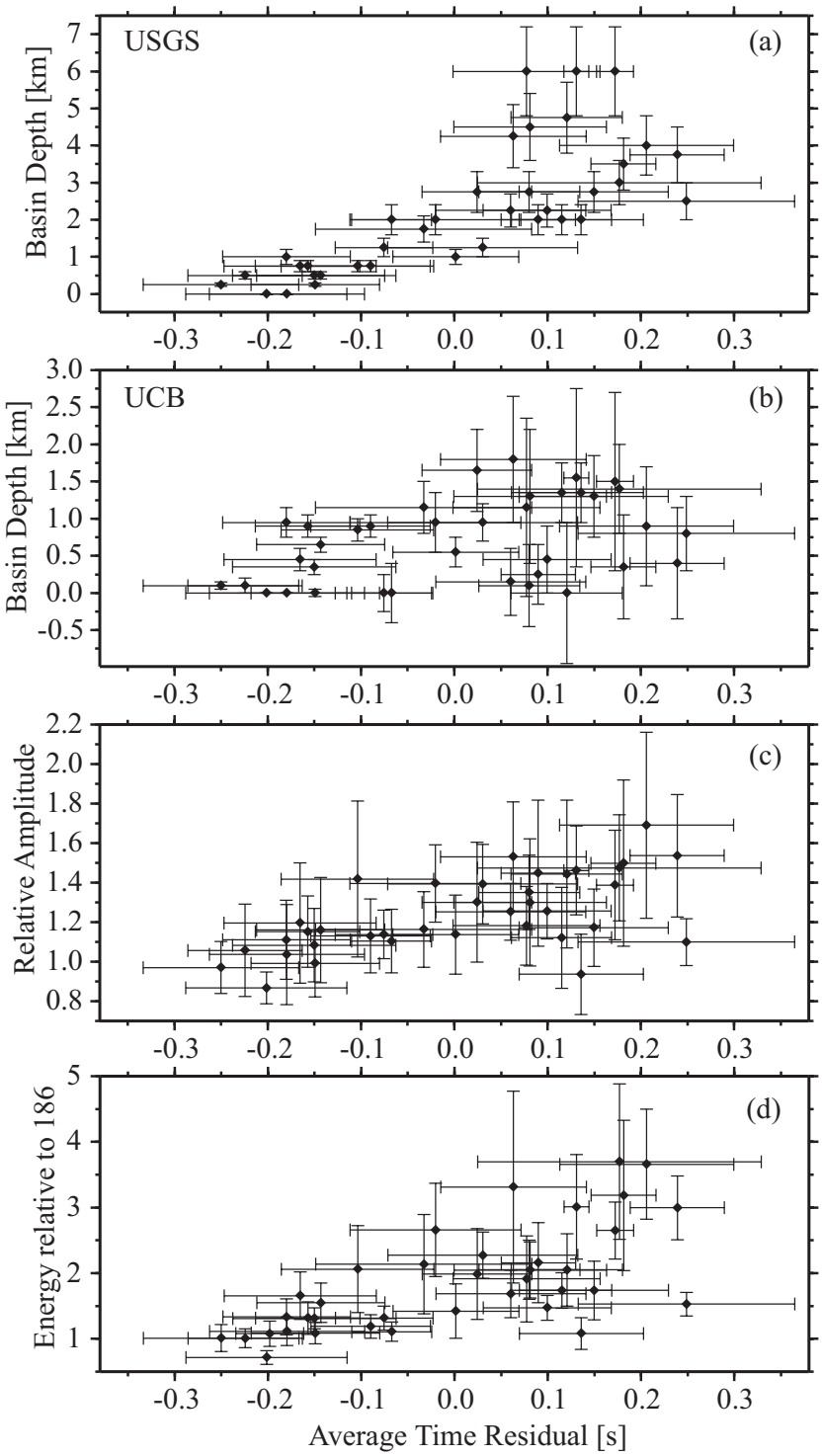

Figure 9. (a) Basin depth from the USGS model as a function of the average time residual measured for the seven teleseismic events. Each data point represents a SCVSE station. (b) Same as in a, except that the basin depth from the UCB model is used. (c) Relative amplitudes as a function of the average time residual for the seven teleseismic events. (d) Average *P*-wave energy for the seven teleseismic events relative to the station 186 as a function of average time residual. Each data point represents a SCVSE station.

ues averaged over the seven teleseismic events as a function of the USGS model basin depth. Stations located above the basin that was shallower than 3 km show a linear relationship between the observed variables and the basin depth. The obtained linear equations fit reasonably well as indicated by the R^2 values. Coefficients of the line fit and their standard errors are included in Figure 10.

Waveform Modeling

So far we only used synthetic waveforms to model *P*-wave arrival-time delay, amplitude, and energy. In the next section we focus on the waveform comparison. The synthetic and recorded waveforms for event 4 at stations 120, 238, 186, and PG2 are presented in Figure 11. Event 4 was

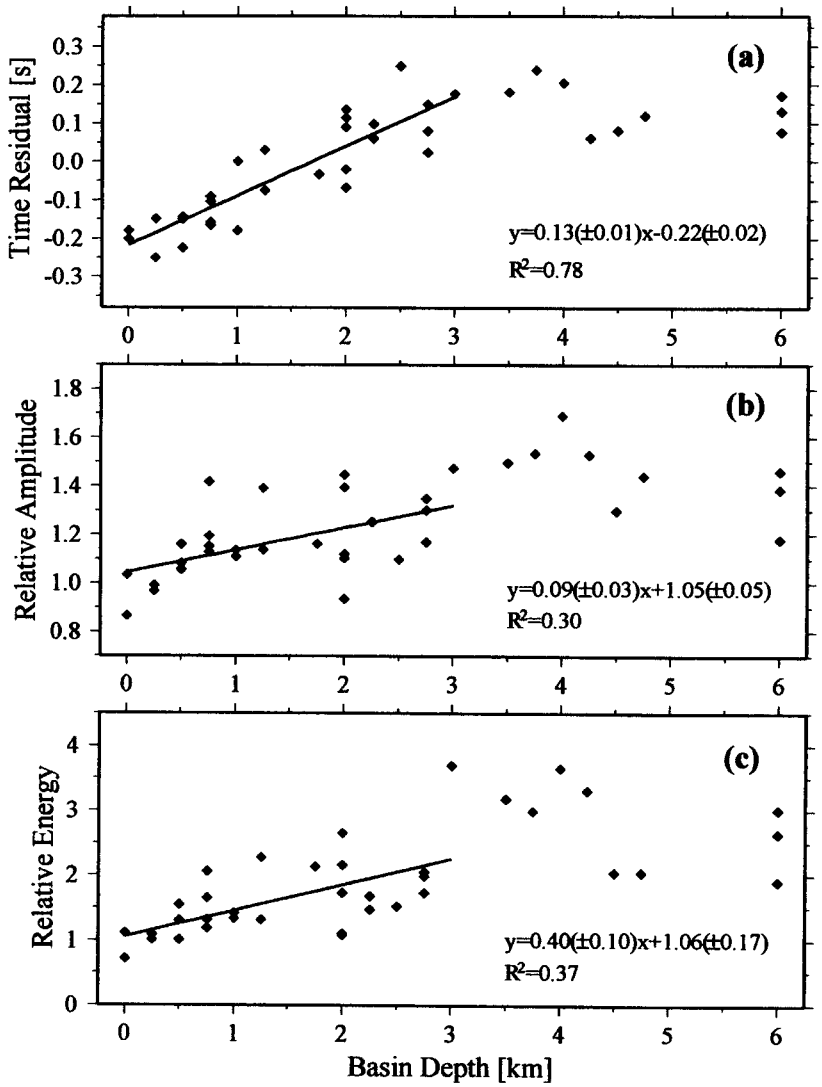

Figure 10. (a) Travel-time residuals averaged over the seven teleseismic events as a function of the USGS model basin depth. Stations located above the basin that was shallower than 3 km were used in the regression. Equations of the line fit and the R^2 value are listed. Standard errors are included in parentheses. (b) Relative amplitudes for the seven teleseismic events as a function of the USGS basin depth. (c) Average *P*-wave energy for the seven teleseismic events as a function of the USGS basin depth.

selected because the beginning of the record is simple with strong and clear *P*- and *pP*-wave arrivals.

The instrument response has been removed and the waveforms have been bandpass filtered between 0.1 and 0.5 Hz with an acausal, four-pole Butterworth filter. The synthetics were constructed by summing the primary *P*-wave response with the *pP*-wave response. The *pP*-delay time and relative amplification of -1.4 measured at station MHC were used to scale the synthetics. Final synthetics for all the stations were shifted by the same time, and the amplitudes for all stations were scaled by the same amount so that the *P*-wave arrivals for station 186 coincided for data and synthetics. Thus, the comparison between the observations and synthetics for stations other than 186 demonstrate model predictions in terms of both time and amplitude. The synthetics agree with the data in terms of amplification and coda generation, but good phase agreement of later arrivals was not possible at all stations. However, phase agreement with the first arrival is very good. Considering that the synthetics are computed solely from the basin response to incident *P* and *pP*, the agreement is quite remarkable.

The waveforms show similarities based on location. Shown are representative stations of the two basins, the region outside the basins, and the ridge in between the basins. Station 120 was located over the Cupertino basin in the UCB and in the USGS model. The observations show amplification of the *P* and *pP* phase as well as large-amplitude *P*-wave coda. These observations are better matched with the UCB model synthetics.

Station 238, located over the Evergreen basin, shows large observed *P*- and *pP*-wave amplifications and *P*-wave coda amplitudes. Overall, the UCB synthetics model the observed waveforms much better.

Station 186 was located outside the Cupertino basin in both models. The observations and synthetics from both models are simple and agree in terms of small *P*-wave amplifications and *P*-wave coda amplitudes.

Station PG2, located between the two basins in both

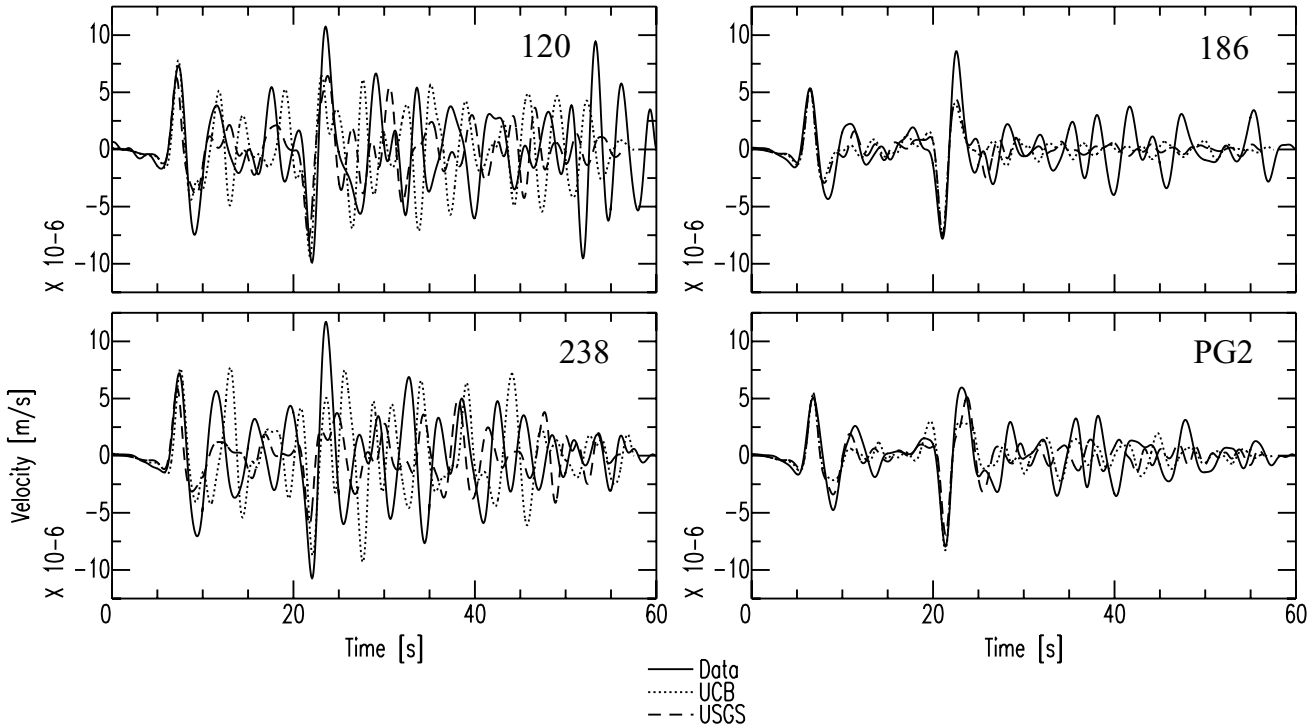

Figure 11. The observed (solid) and calculated waveforms for the UCB (dotted) and the USGS model (dashed) for event 4. Stations 120, 238, 186, and PG2 are shown. The first *P* wave is followed by the *pP* wave about 15 sec later.

models, shows small amplitudes that are well modeled by both velocity models. The observed *P*-wave coda amplitudes are larger then predicted by the two velocity models.

The data recorded at stations above the basins (e.g., stations 120 and 238 in Fig. 11) show strong converted arrivals between the *P* and *pP* waves. These phases are also present in the UCB model synthetics but are much smaller when the USGS model is used. The time delay of the first converted arrival after the *P* wave on station 120 is 4 sec.

To estimate travel-time delays for some of the converted arrivals, we used a cross section of the UCB model across the SCV through station 120 and an incident *P*-wave perpendicular to the basin bottom (Fig. 12). In the UCB model, the depth of the basin under station 120 is $h = 1.4$ km, and the dip of the Cupertino basin in the west is $\alpha = 16.3°$. The results listed in Table 2 indicate that candidate phases for the first converted arrival observed in the data and in the UCB synthetics include *PsSSS*, *PsPSS*, and *PpSSS*.

The UCB model synthetics better match the observed converted arrivals. This suggests that a sharp basin/bedrock velocity contrast that is present in the UCB model is needed to explain the observations. Observations of converted arrivals in the data and the UCB model synthetics indicate that basin-induced converted arrivals could be used further to estimate the sediments thickness. A study by Chen *et al.* (1996) showed that in the case of a wide basin with little lateral variations, *S*- to *P*-converted waves could be used to determine sediments thickness and average shear-wave velocity.

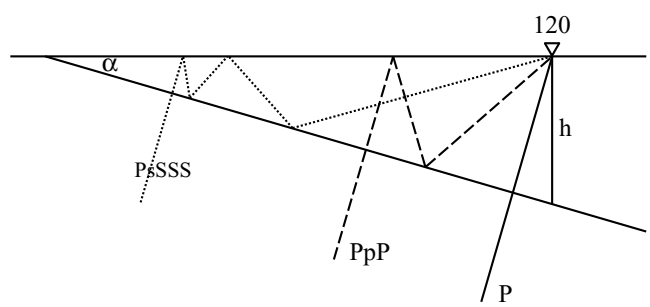

Figure 12. Part of the UCB model cross section across the SCV through station 120, used to estimate travel-time delays for some of the converted arrivals (see Table 2). In the UCB model, the depth of the basin under the station 120 is $h = 1.4$ km, and the dip of the Cupertino basin in the west is $\alpha = 16.3°$. The *P* wave and two converted phases are shown. The incident *P* wave perpendicular to the basin bottom was used in the calculation.

Figure 13 shows the observed waveforms (top) for event 4 recorded on stations 120, 238, 186, and PG2. Shown below are the synthetics calculated by using the UCB model and its variations. From top to bottom they are: the original UCB model, an increase in the *P*-wave velocity in the basins by 25%, an increase in the *S*-wave velocity in the basins by

Table 2
Travel-Time Delays for Some of the Converted Arrivals Relative to *P* Wave at Station 120

Phase	*dt* (sec)	Phase	*dt* (sec)
PpP	1.3	*PpPPP*	1.9
PpS	1.9	*PpPPS*	2.8
PsP	1.7	*PpPSS*	3.3
PsS	2.4	*PsPPS*	2.9
		PpSSS	3.6
		PsPSS	3.5
		PsSSS	3.8

UCB model cross section across the SCV was used in the calculation (see Fig. 12).

25%, and the UCB model without the basins. The synthetics were constructed as described for Figure 11.

The results show that the synthetics obtained with the original UCB model best match the observations. The 25% *P*-wave velocity increase in the basins resulted in smaller amplitudes of the secondary arrivals. The 25% *S*-wave velocity increase in the basins had a similar effect, but it reduced even further the amplitudes of the late arrivals. As expected the UCB model with the SCV basins removed (bottom) resulted in simple waveforms at all stations. Only increases in wave velocity were examined as decreasing seismic velocities in the model would greatly increase memory requirements while maintaining the same maximum computed frequency of the synthetic seismograms.

Conclusions

Our analysis of the teleseismic *P* waves of seven events recorded by the SCVSE demonstrates the influence of the SCV basins on the timing and amplitudes of primary arrivals, and on the generation of a converted wave field. Observed *P*-wave arrival-time delays are on the order of ± 0.25 sec and show the spatial extent of the basins. These arrival-time delays were found to correlate strongly with other observations such as primary *P*-wave amplification (Fig. 9c) and seismic wave energy (Fig. 9d). In fact, a companion paper

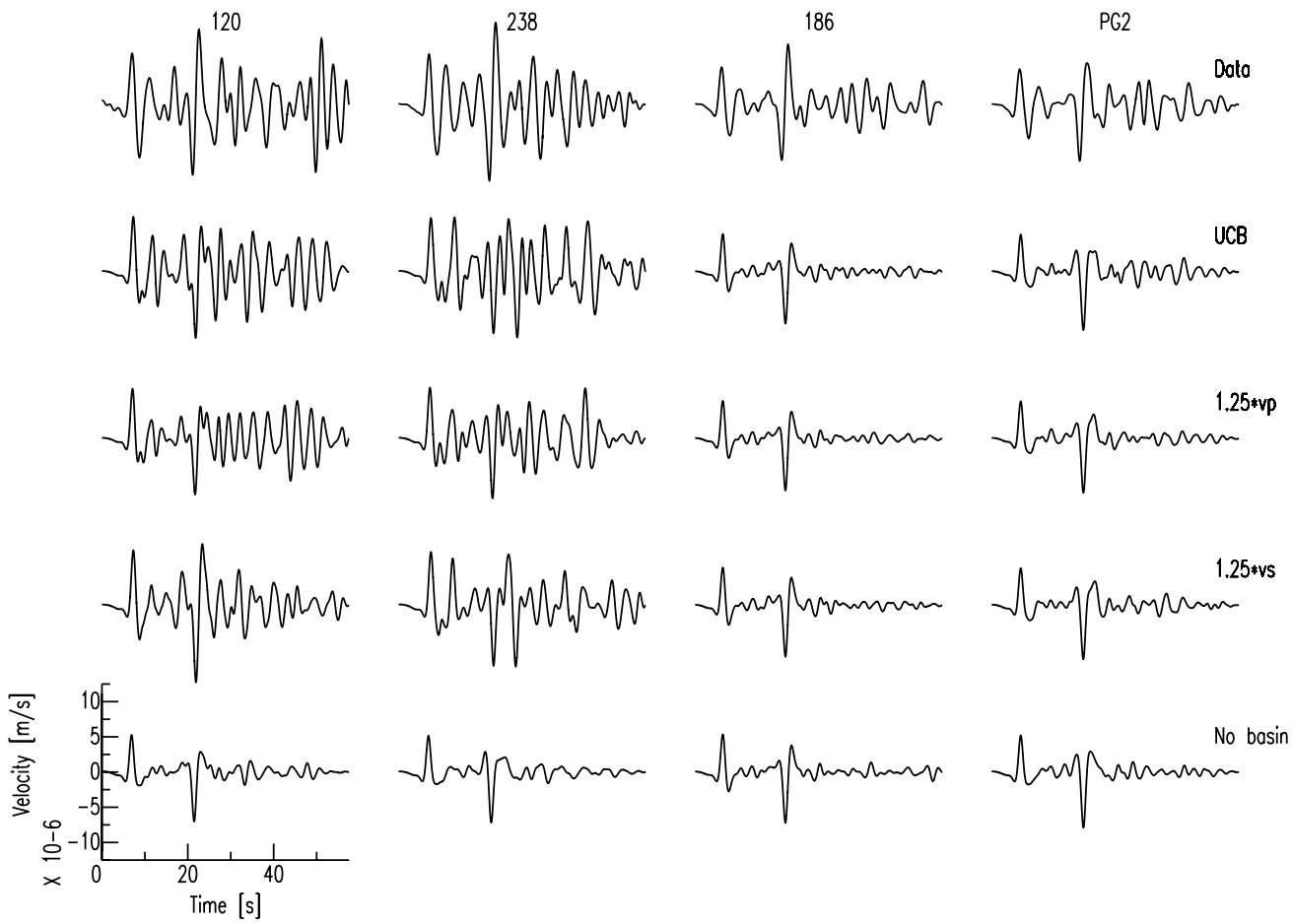

Figure 13. The observed waveforms (top) for event 4 recorded at stations 120, 238, 186, and PG2. Shown below are the calculated waveforms for the UCB model, the UCB model with the 25% increased *P*-wave velocity in the SCV basins, the UCB model with the 25% increased *S*-wave velocity in the SCV basins, and the UCB model with the SCV basins removed.

investigating microseism amplification and dominant period (Dolenc and Dreger, 2005) reveals that these observations are also strongly correlated to the teleseismic arrival-time delays. This diverse data set is strongly influenced by basin structure, indicating that it may be used to invert for refined seismic velocity models.

We also find that the arrival-time delays are correlated with the basin depth as specified in the two 3D seismic velocity models proposed for the region (Figs. 9a,b). The correlation is better for the USGS model. Simulated *P*-wave fields match these observations but, at the same time, indicate that additional modeling is needed to explain the full range of the observations. For example, the spatial correlations indicate that the geometry of the USGS model is superior in terms of the southern extent of the western Cupertino basin, the eastern extent of the eastern Evergreen basin, and the structure of the bedrock ridge between the two deep basins. However, the spatially simpler UCB model tends to explain the primary *P*-wave amplification and converted arrivals better, which appears to be caused by the sharp contrast between basin and basement seismic wave velocity in that model. These results suggest that future work should focus on using the USGS basin geometry with a less strong internal velocity gradient and a sharp internal interface to produce strong converted arrivals.

The teleseismic observations presented in this article and the empirical relationships that have been obtained between the observables and basin depth may be combined with similar empirical relationships for microseism observables and local earthquake low-frequency ($f < 0.3$ Hz) *S*-wave amplification characteristics. This is described in Dolenc and Dreger (2005). With such relationships calibrated to *S*-wave amplification it will be possible to estimate local-earthquake *S*-wave amplification at new sites by temporarily deploying instrumentation to record microseism and teleseismic data. Relating such new observations to a continuously operated reference station (e.g., MHC for the SCV) offers hope that it will be possible to identify site-specific amplification characteristics relatively easily and also interpolate basin structure using the empirically determined relationships.

Acknowledgments

This research was conducted at the UC Berkeley Seismological Laboratory. It was supported by the USGS Grants 99HQGR0057 and 00HQGR0048 and, in part, by The Hellman Faculty Fund. Work was performed under the auspices of the U.S. Department of Energy by the Lawrence Livermore National Laboratory under Contract W-7405-ENG-48.

The finite-difference code E3D was written by Shawn Larsen of Lawrence Livermore National Laboratory. Large-model computations were performed on the supercomputer Fujitsu VPP700E at the Institute of Physical and Chemical Research (RIKEN) in Japan. The UC Berkeley velocity model developed by Christiane Stidham and the USGS ver. 2 velocity model provided by Robert C. Jachens of the U.S. Geological Survey were used. Data recorded during the Santa Clara Valley seismic experiment (SCVSE) and instrument calibrations were made available by Allan G. Lindh of the U.S. Geological Survey. Critical reviews by Joe Fletcher of the U.S. Geological Survey and an anonymous referee greatly improved the manuscript. This is contribution no. 05-05 of the UC Berkeley Seismological Laboratory.

References

Brocher, T. E., E. E. Brabb, R. D. Catchings, G. S. Fuis, T. E. Fumal, R. C. Jachens, A. S. Jayko, R. E. Kayen, R. J. McLaughlin, T. Parsons, M. J. Rymer, R. G. Stanley, and C. M. Wentworth (1997). A crustal-scale 3-D seismic velocity model for the San Francisco Bay area, California, *EOS Trans. AGU.* **78,** F435.

Brocher, T. M., J. McCarthy, P. E. Hart, W. S. Holbrook, K. P. Furlong, T. V. McEvilly, J. A. Hole, and S. L. Klemperer (1994). Seismic evidence for a lower-crustal detachment beneath San Francisco Bay, California, *Science* **265,** 1436–1439.

Cerjan, C., D. Kosloff, R. Kosloff, and M. Reshef (1985). A nonreflecting boundary condition for discrete acoustic and elastic wave equations, *Geophysics* **50,** 705–708.

Chen, K.-C., J.-M. Chiu, and Y.-T. Yang (1996). Shear-wave velocity of the sedimentary basin in the Upper Mississippi Embayment using S-to-P converted arrivals, *Bull. Seism. Soc. Am.* **86,** 848–856.

Clayton, R., and B. Engquist (1977). Absorbing boundary conditions for acoustic and elastic wave equations, *Bull. Seism. Soc. Am.* **67,** 1529–1540.

Dolenc, D. (2001). Basin structure influences on the teleseismic wave propagation in the Santa Clara Valley, California, *M.S. Thesis*, University of California, Berkeley.

Dolenc, D., and D. Dreger (2005). Microseisms observations in the Santa Clara Valley, California, *Bull. Seism. Soc. Am.* **95,** no. 3, 1137–1149.

Dreger, D., and B. Romanowicz (1994). Source characteristics of events in the San Francisco Bay region, *U.S. Geol. Surv. Open-File Rept. 94-176*, 301–309.

Fletcher, J. B., J. Boatwright, and A. G. Lindh (2003). Wave propagation and site response in the Santa Clara Valley, *Bull. Seism. Soc. Am.* **93,** 480–500.

Frankel, A., and J. Vidale (1992). A three-dimensional simulation of seismic waves in the Santa Clara Valley, California, from a Loma Prieta aftershock, *Bull. Seism. Soc. Am.* **82,** 2045–2074.

Frankel, A., D. Carver, E. Cranswick, T. Bice, R. Sell, and S. Hanson (2001). Observations of basin ground motions from a dense seismic array in San Jose, California, *Bull. Seism. Soc. Am.* **91,** 1–12.

Hartzell, S., D. Carver, and R. A. Williams (2001). Site response, shallow shear-wave velocity, and damage in Los Gatos, California, from the 1989 Loma Prieta earthquake, *Bull. Seism. Soc. Am.* **91,** 468–478.

Jachens, R. C., A. Griscom, and C. W. Roberts (1995). Regional extent of Great Valley basement west of the Great Valley, California: implications for extensive tectonic wedging in the California Coast Ranges, *J. Geophys. Res.* **100,** 12,769–12,790.

Jachens, R. C., R. F. Sikora, E. E. Brabb, C. M. Wentworth, T. M. Brocher, M. S. Marlow, and C. W. Roberts (1997). The basement interface: San Francisco Bay area, California, 3-D seismic velocity model, *EOS Trans. AGU.* **78,** F436.

Larsen, S., and C. A. Schultz (1995). ELAS3D: 2D/3D elastic finite-difference wave propagation code, Technical Report No. UCRL-MA-121792, 19 pp.

Levander, A. R. (1988). Fourth-order finite-difference P-SV seismograms, *Geophysics* **53,** 1425–1436.

Lindh, A. G., J. P. Eaton, M. O. Allen, J. H. Healy, S. W. Stewart, and L. Damerell (1999). Calibration formulae and values for velocity seismometers used in the 1998 Santa Clara Valley, California seismic experiment, *U.S. Geol. Surv. Open-File Rept. 99-434*.

Olsen, K. B., and G. T. Schuster (1995). Causes of low-frequency ground motion amplification in the Salt Lake Basin: the case of the vertically incident P wave, *Geophys. J. Int.* **122,** 1045–1061.

Olsen, K. B., J. C. Pechmann, and G. T. Schuster (1995). Simulation of 3D

elastic wave propagation in the Salt Lake Basin, *Bull. Seism. Soc. Am.* **85,** 1688–1710.

Pratt, T. L., T. M. Brocher, C. S. Weaver, K. C. Creager, C. M. Snelson, R. S. Crosson, K. C. Miller, and A. M. Tréhu (2003). Amplification of seismic waves by the Seattle Basin, Washington State, *Bull. Seism. Soc. Am.* **93,** 535–545.

Stidham, C. (1999). Three-dimensional crustal structure influences on wave propagation and generation of strong ground motion in the greater San Francisco Bay region, *Ph.D. Thesis*, University of California, Berkeley.

Stidham, C., M. Antolik, D. Dreger, S. Larsen, and B. Romanowicz (1999). Three-dimensional structure influences on the strong-motion wavefield of the 1989 Loma Prieta earthquake, *Bull. Seism. Soc. Am.* **89,** 1184–1202.

Wentworth, C. M., T. E. Fumal, T. M. Brocher, and E. E. Brabb (1997). The areal distribution of geologic materials and their seismic velocities, San Francisco Bay area, California, *EOS Trans. AGU.* **78,** F436.

Seismological Laboratory
University of California
Berkeley, California 94720
(D.D., D.D.)

Lawrence Livermore National Laboratory
Livermore, California 94551
(S.L.)

Manuscript received 8 April 2004.

Bulletin of the Seismological Society of America, Vol. 95, No. 3, pp. 1137–1149, June 2005, doi: 10.1785/0120040060

Microseisms Observations in the Santa Clara Valley, California

by David Dolenc and Doug Dreger

Abstract We have investigated ground-motion amplification in the Santa Clara Valley (SCV) using microseisms observed during the 1998 deployment of 41 short-period seismometers. The Santa Clara Valley Seismic Experiment (SCVSE) (Lindh *et al.*, 1999; Fletcher *et al.*, 2003) recorded many local, regional, and teleseismic events. In our previous work we investigated the 3D velocity structure of the SCV by modeling the teleseismic *P* waves recorded during the SCVSE (Dolenc *et al.*, 2005). To complement these results, we now focus on the microseisms that were recorded during the same period and relate these observations to local earthquake wave amplification. It is found that the seismic noise is related to the ocean wave heights measured on the weather buoy west of Half Moon Bay, California. The spectral ratio of the horizontal to vertical (H/V) microseisms at each SCVSE site is stable with time, and the period of the dominant peak in the H/V ratio is related to the basin depth. The results of this study show that seismic noise can be used in the assessment of the effects of deep sediments on long-period earthquake ground motions.

Introduction

Santa Clara Valley (SCV) is located south of the San Francisco Bay and comprises two elongated alluvial basins, the Cupertino basin in the west and the Evergreen basin in the east. To learn more about the basin structure, the Santa Clara Valley Seismic Experiment (SCVSE), a joint project of the U.S. Geological Survey (USGS), University of California, Berkeley (UCB), and Incorporated Research Institutions for Seismology Program for Array Seismic Studies of Continental Lithosphere (IRIS PASSCAL), was deployed in the SCV from June through November 1998 (Fig. 1). In our previous work we investigated the 3D velocity structure of the SCV by modeling the teleseismic *P* waves recorded during the SCVSE (Dolenc, 2001; Dolenc *et al.*, 2005). The goal of this study was to demonstrate that the microseisms recorded during the SCVSE are also sensitive to the deep basin structure and can be used to predict the effects of deep sediments on long-period earthquake ground motions.

Microseisms

The microseisms are generated by the pressure variations on the sea floor caused by the ocean waves. These pressure variations are the result of the standing waves and their frequency is twice the frequency of the original traveling ocean waves (Longuet-Higgins, 1950). The microseisms can be observed in the frequency range from 0.1 to 5 Hz.

We examined the relationship between the ocean waves recorded on the buoy west of Half Moon Bay, California, and the microseisms recorded by the SCVSE. The locations of the weather buoy and of the SCV seismic stations are shown in Figure 1. The buoy data were obtained from the National Data Buoy Center and consist of standard meteorological data as well as wind and wave information. In this study we used spectral wave density (SWD), a recorded energy within frequency bins covering the range from 0.03 to 0.4 Hz. Figure 2 shows the spectral wave density in the three frequency bins in July and October 1998. We selected one quiet (26–30 July) and one stormy interval (24–28 October) for further analysis. There were no significant local, regional, or teleseismic events in either of the two 5-day periods.

Figure 3 presents an example of the observed data. The SWD of the ocean waves recorded at the buoy (black) and the power spectral density (PSD) for the seismic data recorded on the vertical components at stations 313 and 098 are shown. The two stations were selected as representatives of stations located close to the ocean (313) and those further inland (098). The PSDs of the seismic data are compared with the ocean-wave data recorded in the half-frequency bin. The moving average over five adjacent data points was applied to buoy and seismic data. The left column shows data for the quiet interval in July 1998 and the right column shows data for the stormy interval in October 1998.

In both cases the seismic noise closely tracks the ocean-wave data. This is true at all the seismic stations. These results confirm that the noise observed at the SCV seismic stations during stormy and quiet periods is related to ocean waves and not to urban noise.

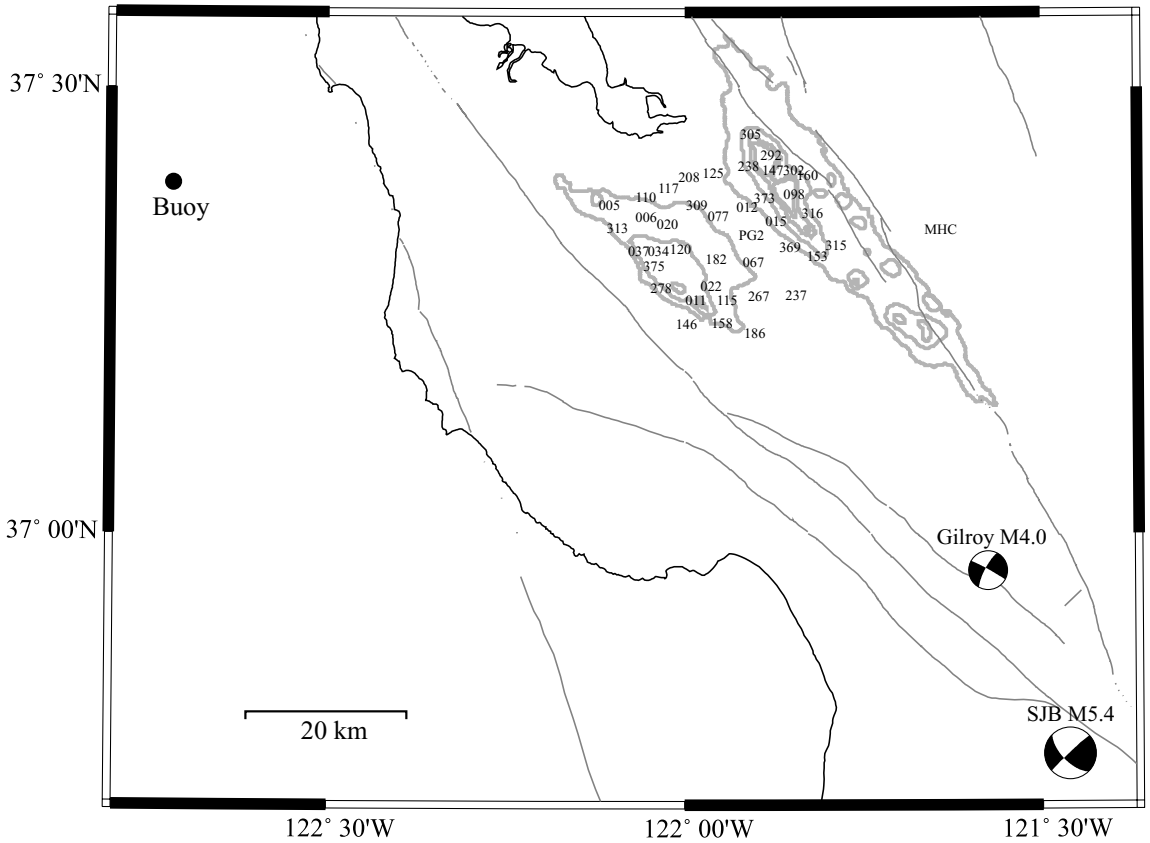

Figure 1. Location of the SCV seismic array south of the San Francisco Bay. Numbers indicate SCVSE seismic stations. Thin gray lines are the active faults in the region, and MHC is a permanent station of the Berkeley Digital Seismic Network. Contours of the basins from the USGS model at 1 km, 3 km, 5 km, and 6 km depth are shown in gray. The circle indicates the location of the weather buoy west of Half Moon Bay, California. Focal mechanisms from the Berkeley Seismological Laboratory Moment Tensor Catalog are shown for the two local events used in this study.

Continuous Excitations of the SCV Basins

To determine whether the effect of the basins can be seen in the recordings of the microseisms, we calculated the average PSD at each station for several days. The vertical component ground-velocity records were processed by deconvolving the reported instrument response parameters (Lindh *et al.*, 1999). For every day, the PSD was calculated for 5-min segments at the beginning of each hour for the vertical seismic data. The results were first averaged over the 0.1- to 1-Hz frequency range and then through the day to obtain a single value for each day.

The relationships between the PSDs at the various sites were remarkably consistent. As an example results from 28 October 1998 are presented in Figure 4. The font styles indicate different seismometer types, and the radii of the circles represent the average PSD values. The values are consistently larger over the two basins and smaller between them. As expected, the values observed in the Cupertino basin, which is closer to the ocean, are larger than in the Evergreen basin. No correlation exists with the seismometer type.

The general pattern of these results is similar to that observed for the average *P*-wave energy of the teleseismic events recorded by the same array (figure 8 in Dolenc *et al.*, 2005). Both data sets indicate that a correlation exists between the observed energy and the outline of the Cupertino and the Evergreen basin.

H/V Spectral Ratio of Microseisms

The use of the spectral ratio between the horizontal and vertical components (H/V ratio) to estimate the site amplification from a single-station noise recording was first proposed by Nakamura (1989). Since then, many studies have used the H/V technique to evaluate site response and identify fundamental resonance frequencies of the sedimentary layers. The H/V technique is most often used to study the response of the shallow structures, mainly the response of the soft soils. Some of the studies also applied the H/V technique to deep basins (Yamanaka *et al.*, 1994; Dravinski *at al.*, 1996; von Seht and Wohlenberg, 1999; Bodin and Horton, 1999; Bodin *et al.*, 2001). Typical period ranges of data used

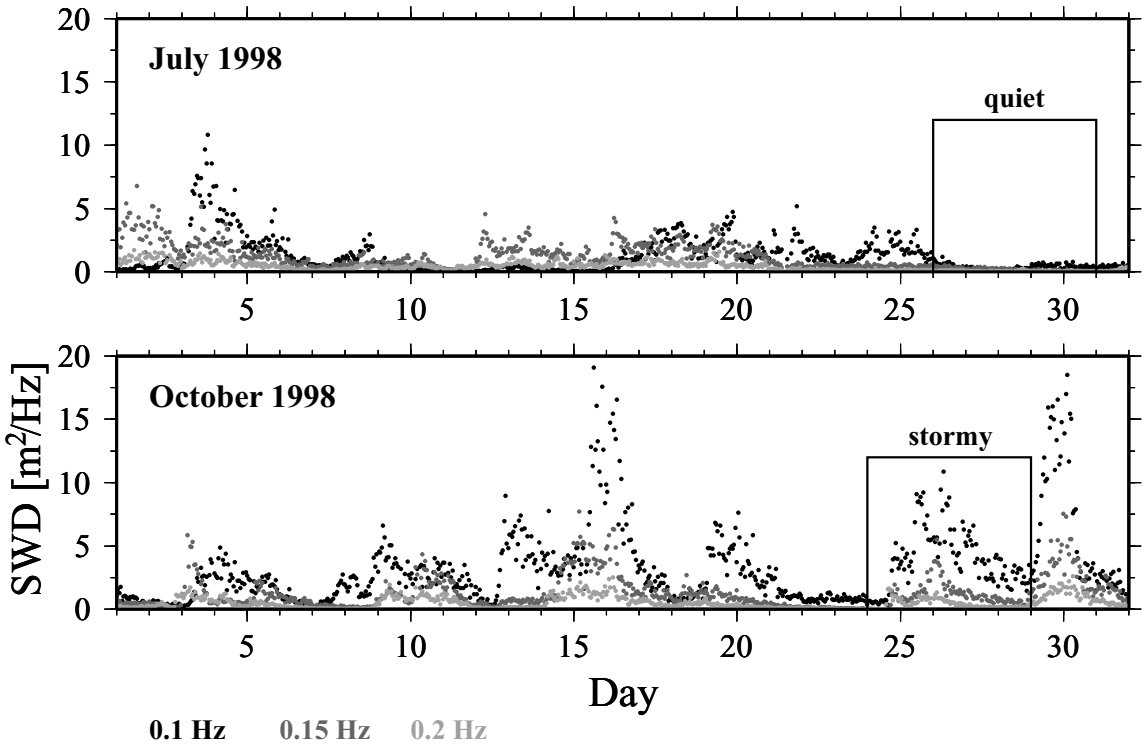

Figure 2. Spectral wave density (SWD) of the ocean waves recorded on the buoy west of Half Moon Bay, California, in July and October 1998. Colors denote 0.1 Hz (black), 0.15 Hz (dark gray), and 0.2 Hz (light gray) frequency bin. The width of each bin was 0.05 Hz.

in shallow-site studies and deep-basin studies are 0.5–2 sec and 2–5 sec, respectively.

We calculated H/V spectral ratios of microseism signals for a 5-day earthquake-free period for each SCV station. The geometric average of the two horizontal components was used to calculate the horizontal spectrum. The H/V spectral ratios for the 5-min segments at the beginning of each hour were calculated. The dominant period of the H/V spectral ratios in the 0.1- to 1-Hz frequency range is stable over time and depends on the location. We show, as examples, the H/V spectral ratios for station 006 located in the northern part of the Cupertino basin, for station 117 at the eastern edge of the Cupertino basin, and for station 208 located between the two basins (Fig. 5). Periods of increased noise for individual time segments are seen as vertical lines in the plots most noticeably in the 0.8- to 1-Hz frequency range. However, the dominant signal that is stable with time can be observed at about 0.2 Hz for station 006, at about 0.35 Hz for station 117, and between 0.35 and 0.6 Hz for station 208. Most of the stations exhibit a similar stable peak between 0.1 and 1 Hz.

To obtain an overall picture we again averaged the H/V spectral ratios calculated for 5-min segments at the beginning of each hour over the 5-day interval. Figure 6 shows results obtained for the quiet interval in July 1998 (dashed) and for the stormy interval in October 1998 (solid). Although the excitation levels for the two intervals were significantly different (Fig. 2), the H/V spectral ratios are very similar. This confirms that the H/V spectral ratios are stable not only during an interval of a few days, but also of a few months. Some of the stations do not show a peak in the 0.1- to 1-Hz frequency range, and this is also observed during both periods.

On some stations different absolute amplitude of the H/V spectral ratios can be observed for the two periods (e.g., stations 098, 125, and 309 in Fig. 6). Because some of the instruments were changed between the two periods we monitored individual instruments to see if amplitude changes could suggest instrumental problems. But we could not identify instruments that would consistently show low H/V spectral ratios. We therefore do not think that the differences are instrument related, but rather that they result from slightly different directionality of the microseisms for the two periods. If this is the case, and assuming that the amplification and interference patterns of the basin 3D structure are direction dependent, this could result in observed changes of absolute amplitudes. The fact that the period of the H/V peak is stable with time and that at the same time we can observe variations in the peak amplitude on some stations suggests that the observed period shifts are first order in nature and amplitude variations of the second order.

The periods of the dominant peak of the H/V spectral ratio in the 0.1- to 1-Hz frequency band appear to be correlated with the two SCV basins (Fig. 7). At the stations

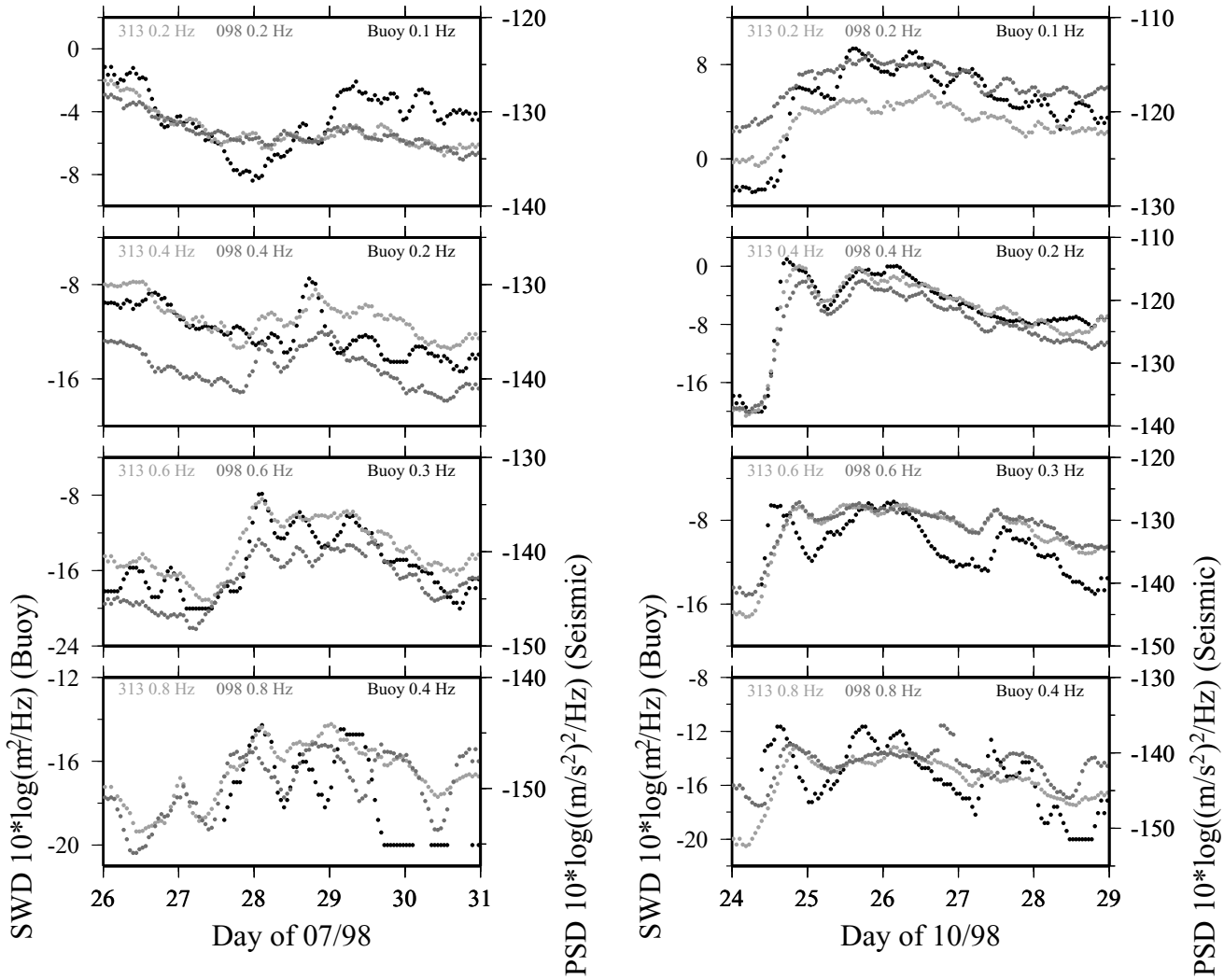

Figure 3. Spectral wave density of the ocean waves (black) and the average PSD for the seismic data in the corresponding double-frequency bin recorded on stations 313 (light gray) and 098 (dark gray). Shown are results for a 5-day period in July 1998 (left) and October 1998 (right).

located above the two basins the dominant peak has longer periods than at the stations located between the basins.

The analysis of the teleseismic *P* waves of seven events recorded by the SCVSE described in a companion study (Dolenc *et al.*, 2005) demonstrated the influence of the SCV basins on the timing of primary arrivals. Observed *P*-wave arrival-time delays were on the order of ± 0.25 sec and showed the spatial extent of the basins. These arrival-time delays were found to correlate strongly with other observations such as primary *P*-wave amplification and seismic wave energy. Here we show that arrival-time delays are also correlated to the dominant period of the microseisms H/V peak. Figures 8a and 8c show the period of the dominant H/V peak in the 0.1- to 1-Hz frequency range as a function of travel-time residuals from the companion paper (Dolenc *et al.*, 2005). The uncertainty of the period of the H/V peak is presented as the width of the H/V peak at 85% of its maximum value. Although we chose this value arbitrarily based on our review of all the data, it is in our opinion a conservative estimate of the possible errors in picking such a peak in the H/V spectra.

In Figures 8a and 8c just the two very different types of observations are compared. Figures 8b and 8d, on the other hand, show the period of the dominant H/V peak in the 0.1- to 1-Hz frequency range in the two intervals as a function of the basin depth as given in the USGS model (Brocher *et al.*, 1997; Jachens *et al.*, 1997). The USGS model and the steps used to determine the USGS model basin depths are described in Dolenc *et al.* (2005).

The correlation is clear between the period of the dominant H/V peak in the 0.1- to 1-Hz frequency range and the basin depth up to 3 km depth. This suggests that the H/V method can be used to determine and constrain the deep structure of the alluvial basins. The best-fit line in Figures

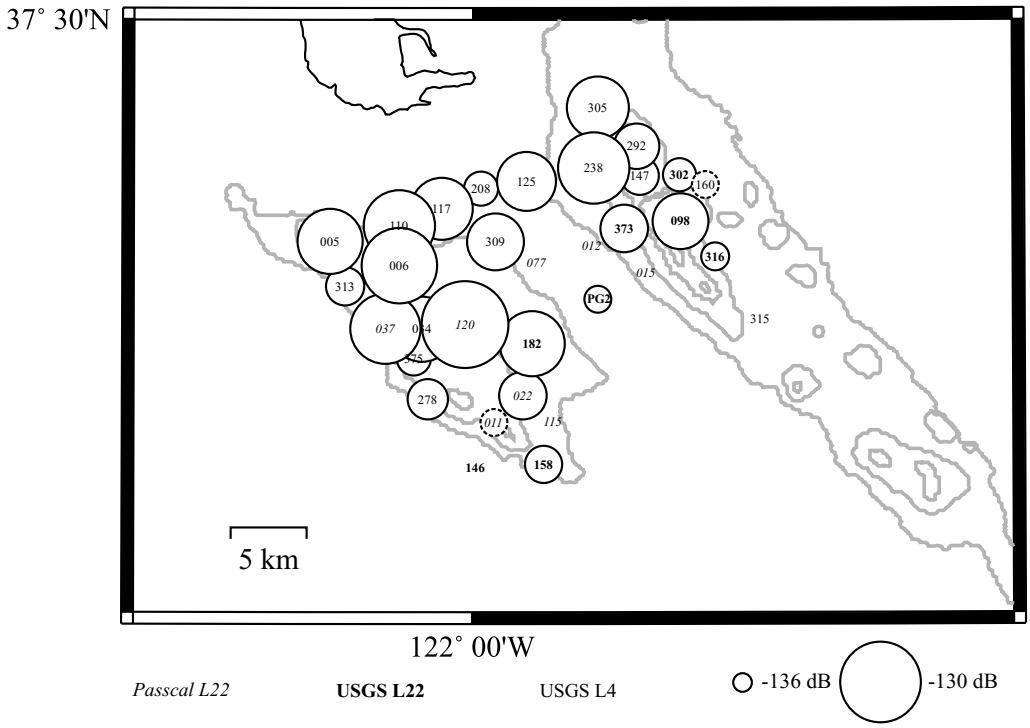

Figure 4. The PSD averaged over the 0.1- to 1-Hz range and over the 5-min segments at the beginning of every hour on 28, October 1998. The font styles indicate the seismometer model. Only values for the stations with complete data on this day are shown. The average PSD at the stations 011 and 160 was −137.05 dB and −138.96 dB, which would result in the circle smaller than the station label. A larger circle (dotted) is shown instead.

8b and 8d is shown for the stations located above basins shallower than 3 km. The 3-km depth for the best-fit line was selected to match the teleseismic observations (figure 10 in Dolenc *et al.*, 2005) and local earthquake observations (figure 9a, b, right columns). The uncertainty in the basin depth is estimated to be 20% of the depth (Jachens *et al.*, 1997).

Some studies have used H/V ratios to predict amplification of ground motion at the specific sites. Lermo and Chávez-García (1994) have shown that Nakamura's technique (Nakamura, 1989) can be used to obtain a rough estimate of the amplification of seismic waves but only when the local geology is simple. Theoretical investigations (Lachet and Bard, 1994; Dravinski *et al.*, 1996), on the other hand, have shown that the H/V method is efficient for estimating the fundamental frequency of a sedimentary site, but that the H/V ratio is not adequate for estimating ground-motion amplification in deep sedimentary basins.

The amplitudes of the H/V peaks for the two 5-day intervals as a function of the basin depth from the USGS velocity model are shown in Figure 10. The mean value and standard deviation are presented for each station. Standard deviation is obtained from averaging H/V ratios for every hour, at the period of the final H/V maximum. The results show that there is a very weak inverse correlation, if any, between the amplitudes of the H/V spectral ratios and the basin depth. Slightly larger H/V amplitudes can be observed at the stations over basins shallower than 2 km. However, considering the uncertainty in the observations and basin depth, there does not appear to be any correlation of H/V amplitude with basin depth. Similarly, when the amplitudes of H/V peaks are plotted as a function of the teleseismic delay times, no correlation is observed.

Ground Motions from Local Earthquakes

One of our objectives is to find relationships between the seismic observables and basin thickness. It is also of primary interest to obtain such relations for local earthquake wave amplification.

The two strongest local earthquakes recorded during the SCV seismic experiment were the San Juan Bautista (SJB, 12 August 1998; M_L 5.4; depth, 9 km) and the Gilroy (10 October 1998; M_L 4.0; depth, 6.5 km) event. Their locations and focal mechanisms are shown in Figure 1.

To measure the incoming seismic wave energy, the vertical and horizontal waveforms were squared and integrated for the 125 sec after the *P*-wave arrival. Peak ground velocity (PGV) recorded on the vertical and horizontal components was also measured. The horizontal component that was

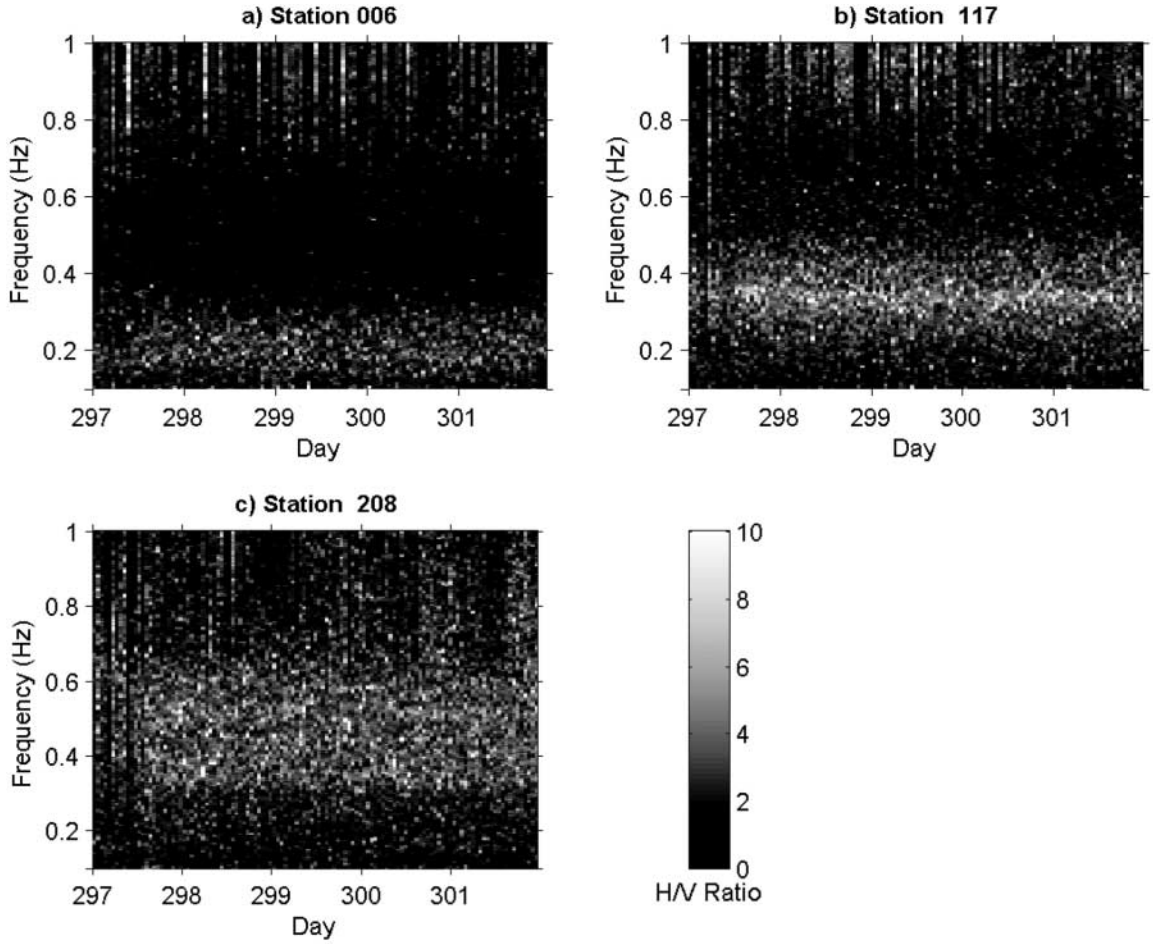

Figure 5. H/V spectral ratio for the stations 006, 117, and 208 as a function of frequency and time. Results for a 5-day interval (24–28 October 1998) are shown.

used was always the vector sum of the two horizontal channels. Results for the Gilroy and SJB events are shown in Figure 10a and 10b. Waveforms were bandpass filtered between 0.1 and 0.3 Hz. This band is used because more systematic results were obtained than in the full-bandwidth case (0.1 to 1 Hz). This is likely because at local distances peak ground motions at short periods are caused by body waves that interact with mid- and lower-crust structure. By examining the lower frequencies, surface waves in the local earthquake records are enhanced and a comparison between local earthquake surface waves and microseism waves is more justified. In both figures the panels on the left show the results as a function of the travel-time residuals from the analysis of the recorded teleseismic events (Dolenc *et al.*, 2005). Panels on the right show the results as a function of the basin depth from the USGS velocity model. Stations above basins shallower than 3 km were used in the regression. The equations of the best-fit lines and the R^2 values are listed in the figures and standard errors are included in parentheses.

Results from the two local events show that the seismic wave energy and PGV for vertical and horizontal components increase with the measured travel-time delays determined from the teleseismic events and with the basin depth from the USGS model. The overall range in PGV amplification in the 0.1- to 0.3-Hz band is about a factor of 2 over the 4-km range. The correlation of local earthquake PGV saturates for basin depths greater than 4 km, similar to what was observed previously for the microseisms (3 km) and the teleseismic observations (3 km) (Dolenc *et al.*, 2005).

1D Modeling

We modeled the response of the sedimentary layers using the propagator matrix approach (Kennett and Kerry, 1979) and the 1D structures below each SCV seismic station taken from the 3D USGS model and from the 3D UCB model (Stidham, 1999; Stidham *et al.*, 1999). In the USGS model, layers with $v_s < 0.5$ km/sec were not incorporated into the 1D models and the attenuation was taken from the original USGS model. There is almost no variability across the entire SCVSE array in the original USGS model in the shallowest three layers. Because the model is almost flat for $v_s < 0.5$ km/sec, these shallow layers should not add to the site-by-site variability in the modeled results. Because attenuation

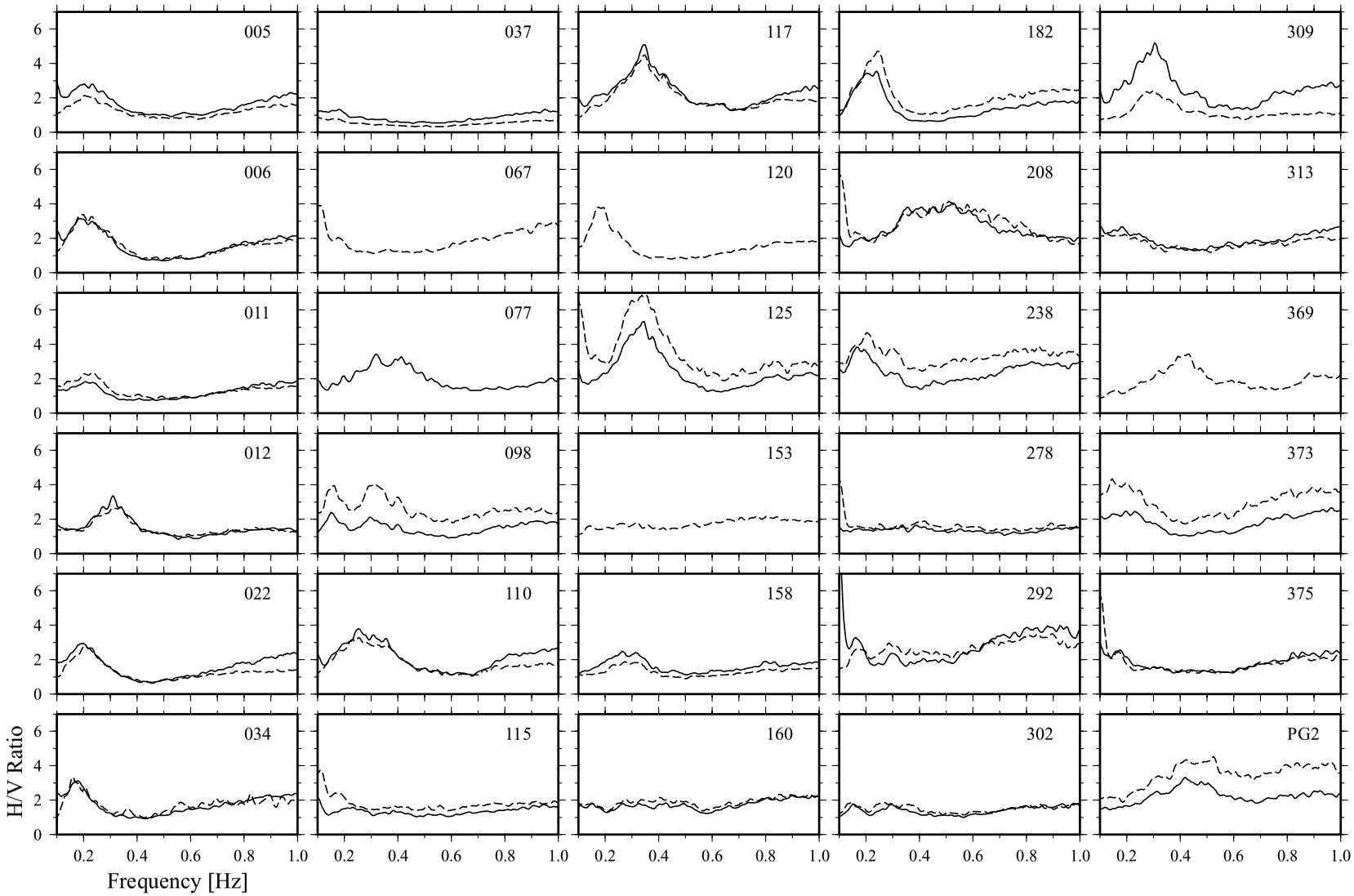

Figure 6. H/V spectral ratio for most of the SCV stations calculated for the 5-day interval in July 1998 (dashed) and October 1998 (solid). For a few stations data were only available for one of the periods.

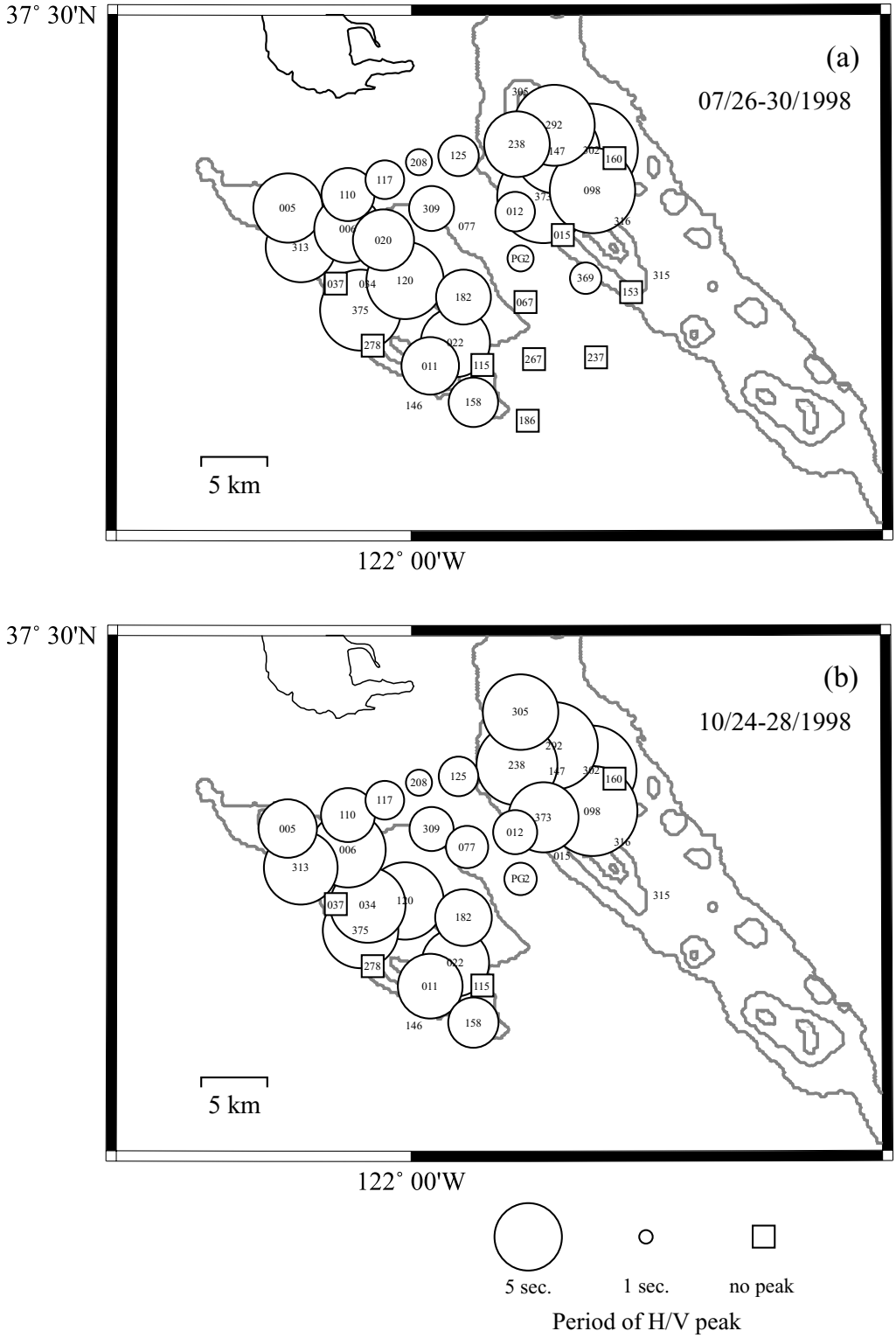

Figure 7. The periods of the H/V spectral peaks in the 0.1- to 1-Hz frequency range for the 5-day period in July 1998 (a) and October 1998 (b). The numbers indicate locations of the SCV seismic stations and the circles indicate the periods of the H/V spectral peaks. Stations that showed no peak in the 0.1- to 1-Hz frequency range are indicated by squares. Contours of the basins from the USGS model at 1 km, 3 km, 5 km, and 6 km are shown in gray.

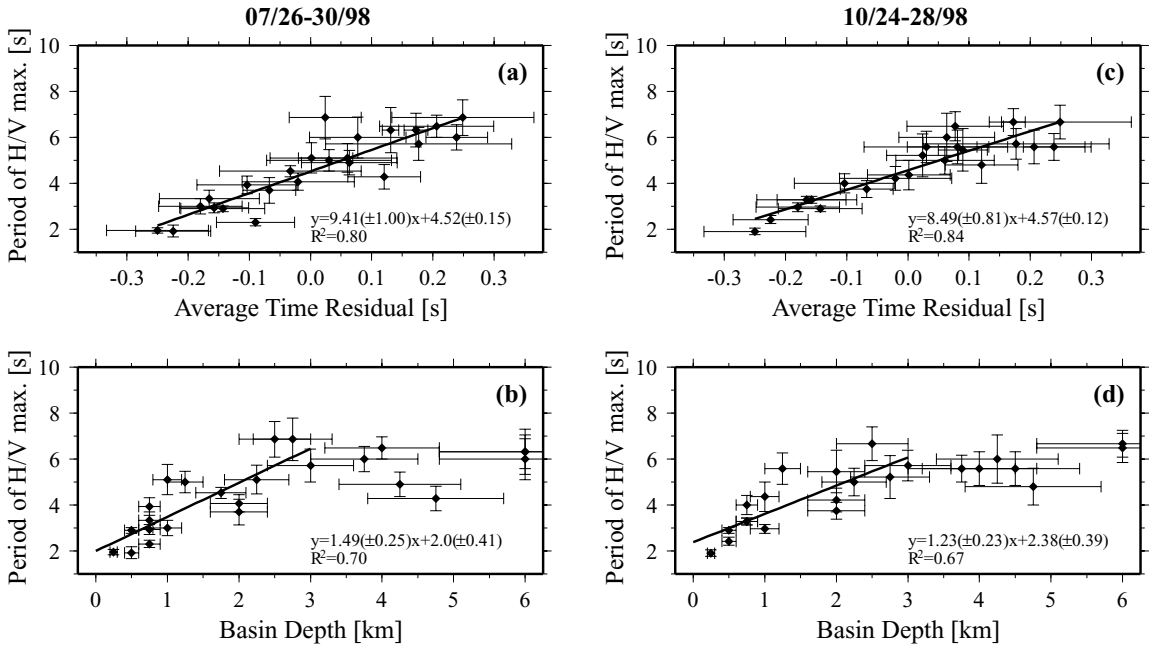

Figure 8. (a,c) The period of the dominant H/V peak in the 0.1- to 1-Hz frequency range as a function of travel-time residuals from the analysis of the recorded teleseismic events (Dolenc *et al.*, 2005). Results for the two 5-day periods are shown. (b,d) The period of the dominant H/V peak in the 0.1- to 1-Hz frequency range as a function of the basin depth from the USGS model for the two 5-day periods. Stations located above basins shallower than 3 km were used in regression. Equations of the line fit and the R^2 values are listed. Standard errors are included in parentheses.

is not included in the 3D UCB model, we used values from layers with similar properties from the USGS model. This resulted in a uniform quality factor $Q_s = 50$ within the basin in the 1D UCB models. A propagator matrix method was used to calculate the transfer function of the basin sedimentary layers for the vertical and horizontal component of ground motion.

In Figure 11, the calculated H/V spectral ratios for stations 006, 110, 117, and 208 are compared with the observed H/V ratios at these stations. These four stations are located in the northern part of the SCV (Fig. 1). In both models the basin depth decreases from station 006 located above Cupertino basin, to station 208, located in between the basins. The 1D profiles of the shear-wave seismic velocity below these four stations are shown in Figure 11.

The results show that for some stations the calculated H/V peak period matches the observed H/V peak period (station 006, USGS model). As the basin depth decreases, the H/V peak widens and moves toward higher frequencies. The same trend can be observed for calculated synthetics. For some stations neither of the two models matches the observed H/V peak. This is not surprising, because the basin's complex 3D structure should have a significant effect and should be included in the modeling. Also, the transfer functions of the sedimentary layers were calculated for a simple plane wave and not for a true microseism source.

It may be possible to use the SCV seismic array to locate the microseism sources and then use the 3D finite-difference code to simulate the response of the basins. If possible this will allow for the inversion of microseismic data for 3D basin structure. These possibilities are presently being investigated.

Conclusions

The seismic noise recorded on the SCV seismic stations is related to the energy of the ocean waves observed on the buoy west of Half Moon Bay, California. The period of the microseisms H/V spectral peak in the 1- to 10-sec range is correlated with the depth of the SCV basin beneath the array. The H/V spectral peaks are stable with time and can be observed during both quiet and stormy intervals. Measured energy and PGV for the two local events recorded with the SCV seismic array also show correlation with the depth of the basin beneath the station.

We calculated empirical relationships between the seismic observations and the basin depth. The data in this article, the companion article (Dolenc *et al.*, 2005), and the accompanying empirical relations may be used to further revise and validate basin structure in the SCV. A consistent observation in this study and the companion article (Dolenc *et al.*, 2005) is that the seismic observables saturate for basin depths greater than 3–4 km. Although gravity data indicate a density contrast defining the basins extends to greater

(a)

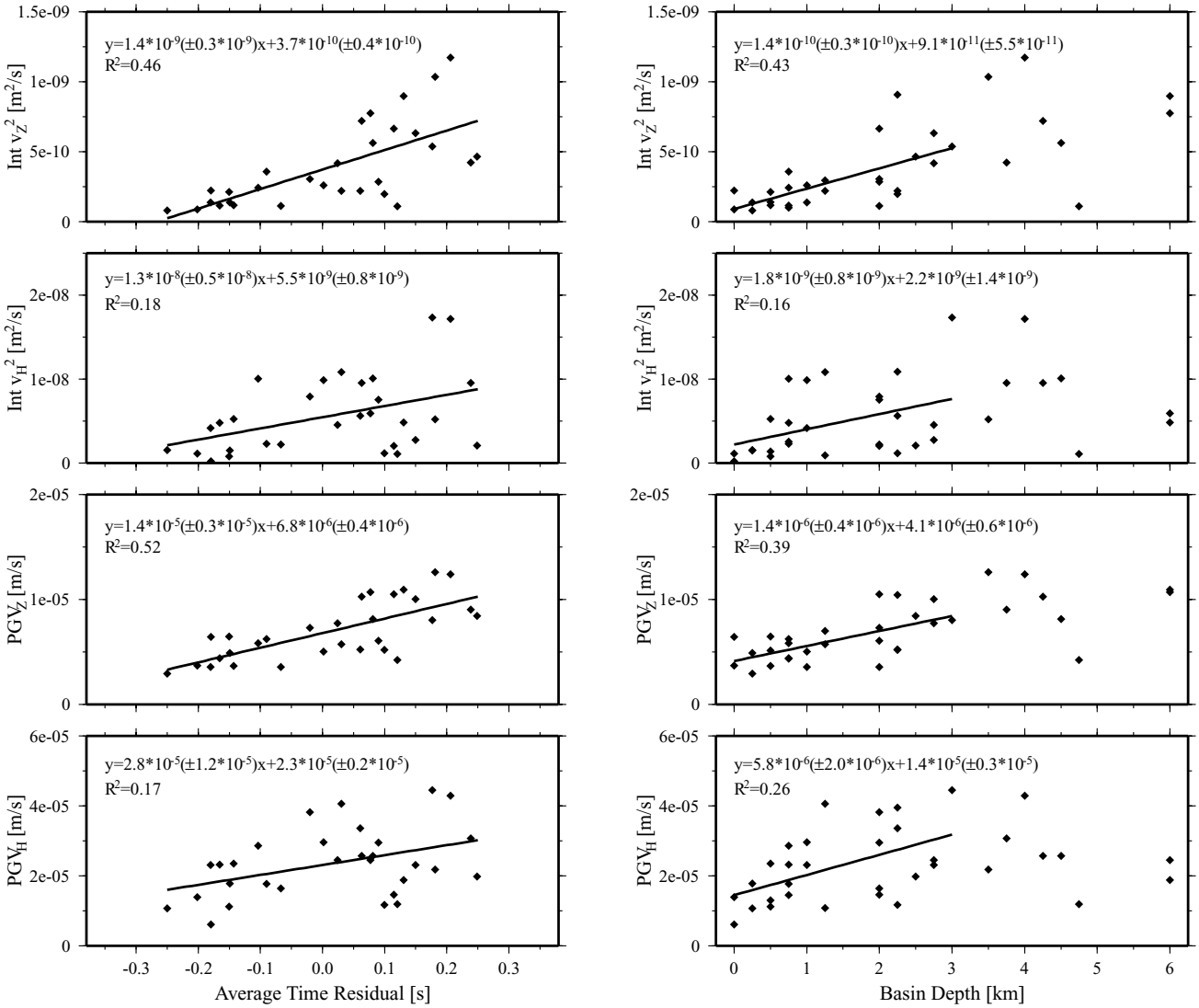

Figure 9. (a) Integrated squared velocity for the 125 sec after the *P*-wave arrival and the PGV measured for the Gilroy M_L 4.0 event. Results for the vertical and for the horizontal component are shown. The horizontal component that was used was always the vector sum of the two horizontal channels. Panels on the left show the results as a function of the travel-time residuals from the analysis of the recorded teleseismic events (Dolenc *et al.*, 2005). Panels on the right show the results as a function of the basin depth from the USGS velocity model. Waveforms were bandpass filtered between 0.1 and 0.3 Hz. The equations of the line fit and the R^2 values are listed. Standard errors are included in parentheses. (b) Same as for a, only for the San Juan Bautista, M_L 5.4 event. (*continued*)

depth in some places (Brocher *et al.*, 1997; Jachens *et al.*, 1997), our results indicate that it is the shallow part of the basins that most significantly affect the seismic wave fields.

Acknowledgments

This research was conducted at the UC Berkeley Seismological Laboratory. It was supported by USGS Grants 99HQGR0057 and 00HQGR0048 and, in part, by The Hellman Faculty Fund.

The UCB velocity model developed by Christiane Stidham and the USGS Ver. 2 velocity model provided by Robert C. Jachens of the U.S. Geological Survey were used. Propagator matrix program written by Lane Johnson of the Lawrence Berkeley National Laboratory was used to calculate the transfer function of the sedimentary layers. Data recorded during the Santa Clara Valley seismic experiment (SCVSE) and instrument calibrations were made available by Allan G. Lindh of the U.S. Geological Survey. Ocean wave data were obtained from the National Data Buoy Center. This is contribution no. 05-06 of the UC Berkeley Seismological Laboratory.

(b)

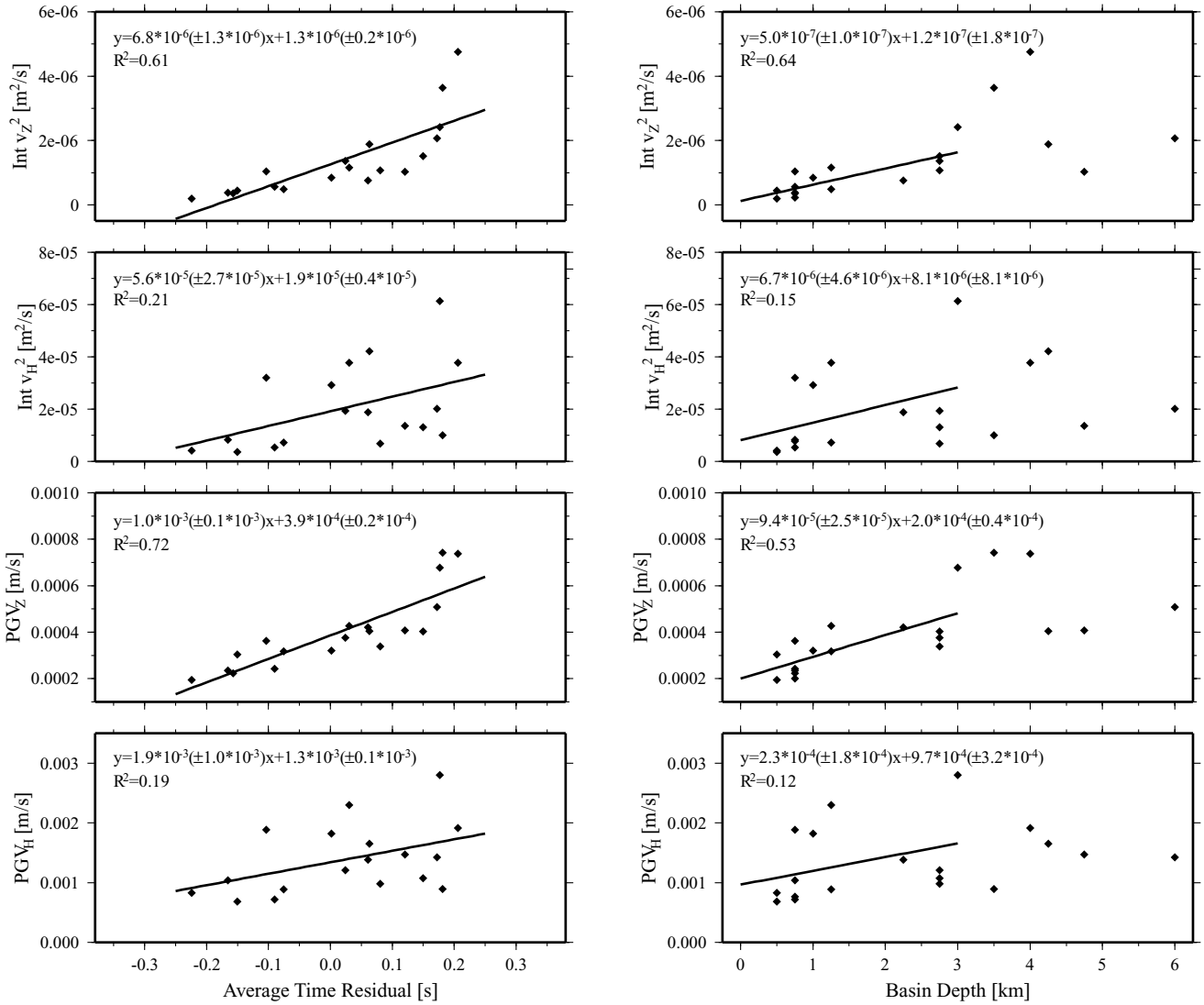

Figure 9. Continued

References

Bodin, P., and S. Horton (1999). Broadband microtremor observation of basin resonance in the Mississippi embayment, Central U.S., *Geophys. Res. Lett.* **26,** 903–906.

Bodin, P., K. Smith, S. Horton, and H. Hwang (2001). Microtremor observations of deep sediment resonance in metropolitan Memphis, Tennessee, *Eng. Geol.* **62,** 159–168.

Brocher, T. E., E. E. Brabb, R. D. Catchings, G. S. Fuis, T. E. Fumal, R. C. Jachens, A. S. Jayko, R. E. Kayen, R. J. McLaughlin, T. Parsons, M. J. Rymer, R. G. Stanley, and C. M. Wentworth (1997). A crustal-scale 3-D seismic velocity model for the San Francisco Bay area, California, *EOS Trans. AGU.* **78,** F435.

Dolenc, D. (2001). Basin structure influences on the teleseismic wave propagation in the Santa Clara Valley, California, *M.S. Thesis*, University of California, Berkeley.

Dolenc, D., D. Dreger, and S. Larsen (2005). Basin structure influences on the propagation of teleseismic waves in the Santa Clara Valley, California, *Bull. Seism. Soc. Am.* **95,** no. 3, 1120–1136.

Dravinski, M., G. Ding, and K.-L. Wen (1996). Analysis of spectral ratios for estimating ground motion in deep basins, *Bull. Seism. Soc. Am.* **86,** 646–654.

Fletcher, J. B., J. Boatwright, and A. G. Lindh (2003). Wave propagation and site response in the Santa Clara Valley, *Bull. Seism. Soc. Am.* **93,** 480–500.

Jachens, R. C., R. F. Sikora, E. E. Brabb, C. M. Wentworth, T. M. Brocher, M. S. Marlow, and C. W. Roberts (1997). The basement interface: San Francisco Bay area, California, 3-D seismic velocity model, *EOS Trans. AGU.* **78,** F436.

Kennett, B. L. N., and N. J. Kerry (1979). Seismic waves in a stratified half space, *Geophys. J. R. Astr. Soc.* **57,** 557–583.

Lachet, C., and P.-Y. Bard (1994). Numerical and theoretical investigations on the possibilities and limitations of Nakamura's technique, *J. Phys. Earth* **42,** 377–397.

Lermo, J., and F. J. Chávez-García (1994). Are microtremors useful in site response evaluation?, *Bull. Seism. Soc. Am.* **84,** 1350–1364.

Lindh, A. G., J. P. Eaton, M. O. Allen, J. H. Healy, S. W. Stewart, and L. Damerell (1999). Calibration formulae and values for velocity seis-

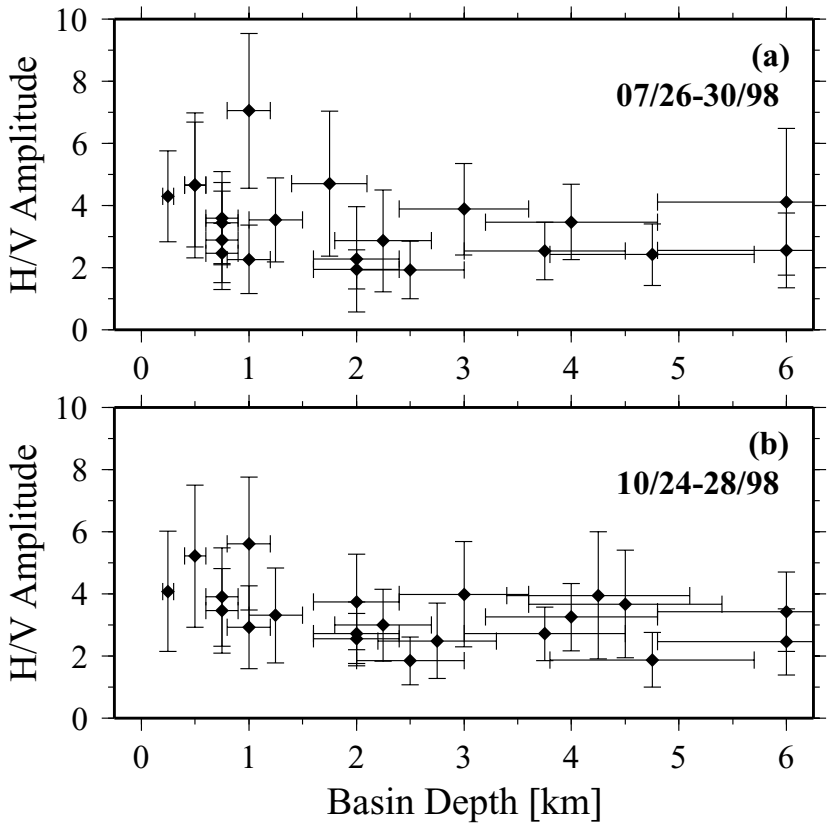

Figure 10. The amplitudes of the H/V peaks as a function of the basin depth from the USGS velocity model. Results for the two 5-day periods are shown.

mometers used in the 1998 Santa Clara Valley, California seismic experiment, *U.S. Geol. Surv. Open-File Rept. 99-434*.

Longuet-Higgins, M. S. (1950). A theory of the origin of microseisms, *Philos. Trans. R. Soc. London Ser. A* **243,** 1–35.

Nakamura, Y. (1989). A method for dynamic characteristics estimation of subsurface using microtremor on the ground surface, *Q. Rep. Railway Tech. Res. Inst. Tokyo* **30,** 25–33.

Stidham, C. (1999). Three-dimensional crustal structure influences on wave propagation and generation of strong ground motion in the greater San Francisco Bay region, *Ph.D. Thesis*, University of California, Berkeley.

Stidham, C., M. Antolik, D. Dreger, S. Larsen, and B. Romanowicz (1999). Three-dimensional structure influences on the strong-motion wavefield of the 1989 Loma Prieta earthquake, *Bull. Seism. Soc. Am.* **89,** 1184–1202.

von Seht, M. I., and J. Wohlenberg (1999). Microtremor measurements used to map thickness of soft sediments, *Bull. Seism. Soc. Am.* **89,** 250–259.

Yamanaka, H., M. Takemura, H. Ishida, and M. Niwa (1994). Characteristics of long-period microtremors and their applicability in exploration of deep sedimentary layers, *Bull. Seism. Soc. Am.* **84,** 1831–1841.

Seismological Laboratory
University of California
Berkeley, California 94720

Manuscript received 8 April 2004.

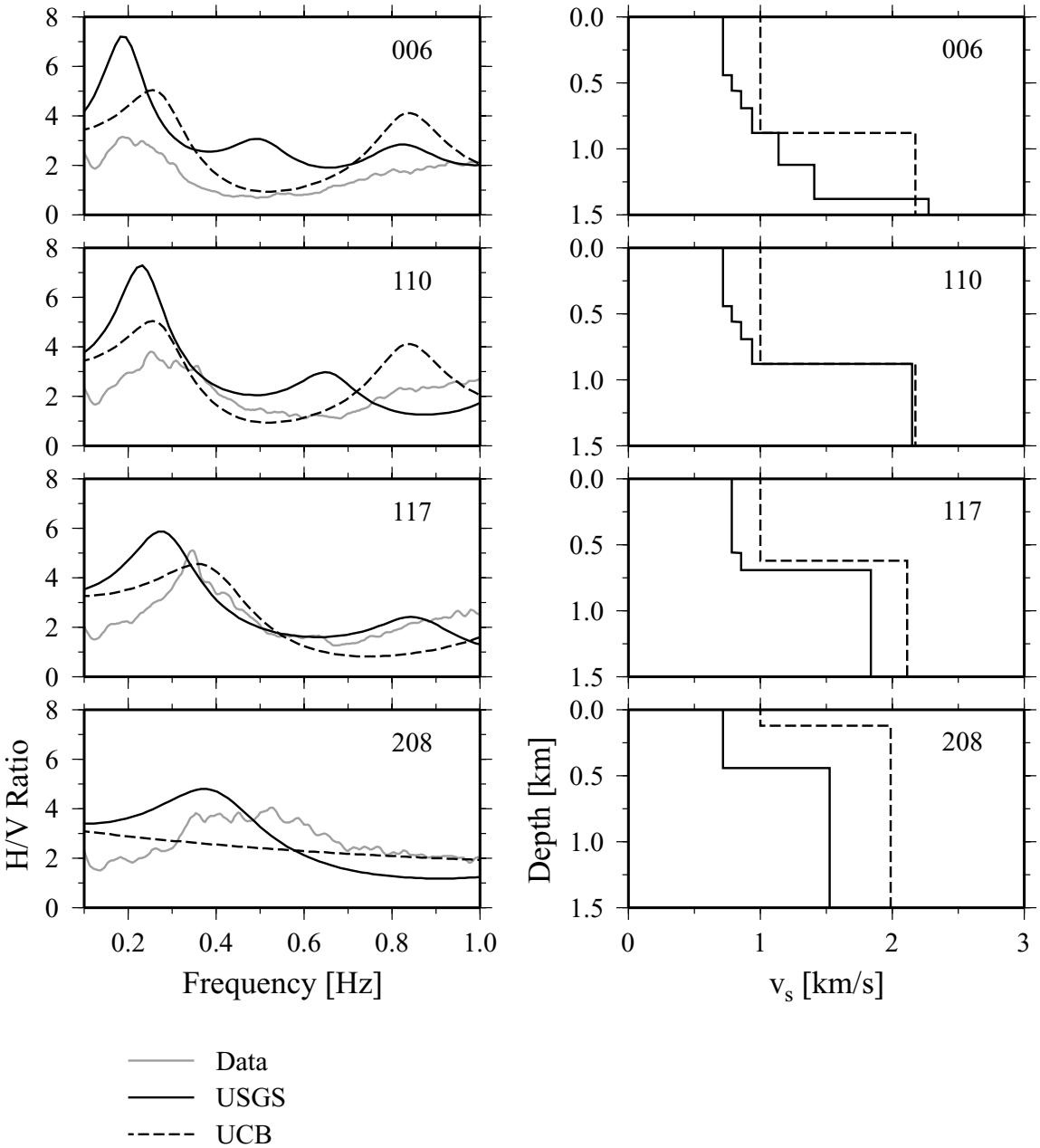

Figure 11. (Left) The calculated H/V spectral ratios for four SCVSE stations obtained with the USGS model (black, solid line) and the UCB model (black, dashed line), compared with the observed H/V spectral ratios (gray) measured during the 5-day interval in October 1998. (Right) Shear-wave seismic velocity (v_s) below selected SCV stations as obtained from the USGS model (solid) and UCB model (dashed). The USGS model layers with $v_s < 0.5$ km/sec were not used in the 1D model.